El Niño–Like Physical and Biogeochemical Ocean Response to Tropical Eruptions

YASSIR A. EDDEBBAR

Scripps Institution of Oceanography, University of California, San Diego, La Jolla, California

KEITH B. RODGERS[a]

Atmospheric and Ocean Sciences Program, Princeton University, Princeton, New Jersey

MATTHEW C. LONG

National Center for Atmospheric Research, Boulder, Colorado

ANEESH C. SUBRAMANIAN,[b] SHANG-PING XIE, AND RALPH F. KEELING

Scripps Institution of Oceanography, University of California, San Diego, La Jolla, California

(Manuscript received 17 July 2018, in final form 22 December 2018)

ABSTRACT

The oceanic response to recent tropical eruptions is examined in Large Ensemble (LE) experiments from two fully coupled global climate models, the Community Earth System Model (CESM) and the Geophysical Fluid Dynamics Laboratory Earth System Model (ESM2M), each forced by a distinct volcanic forcing dataset. Following the simulated eruptions of Agung, El Chichón, and Pinatubo, the ocean loses heat and gains oxygen and carbon, in general agreement with available observations. In both models, substantial global surface cooling is accompanied by El Niño–like equatorial Pacific surface warming a year after the volcanic forcing peaks. A mechanistic analysis of the CESM and ESM2M responses to Pinatubo identifies remote wind forcing from the western Pacific as a major driver of this El Niño–like response. Following eruption, faster cooling over the Maritime Continent than adjacent oceans suppresses convection and leads to persistent westerly wind anomalies over the western tropical Pacific. These wind anomalies excite equatorial downwelling Kelvin waves and the upwelling of warm subsurface anomalies in the eastern Pacific, promoting the development of El Niño conditions through Bjerknes feedbacks a year after eruption. This El Niño–like response drives further ocean heat loss through enhanced equatorial cloud albedo, and dominates global carbon uptake as upwelling of carbon-rich waters is suppressed in the tropical Pacific. Oxygen uptake occurs primarily at high latitudes, where surface cooling intensifies the ventilation of subtropical thermocline waters. These volcanically forced ocean responses are large enough to contribute to the observed decadal variability in oceanic heat, carbon, and oxygen.

1. Introduction

In the absence of global-scale geoengineering experiments, explosive volcanic eruptions represent the closest analogs to radiative management proposals. Following an eruption, the ejection of sulfates into the stratosphere and their consequent aerosol scattering of shortwave radiation increase planetary albedo, driving significant cooling of the troposphere (Pollack et al. 1976; Dutton and Christy 1992; Robock 2000). These radiative perturbations have profound and long-lasting impacts on the climate system, particularly in the ocean where the responses are expected to persist well beyond the *e*-folding lifetime of aerosols (Gleckler et al. 2006; Stenchikov et al. 2009; Schneider et al. 2009; Slawinska and Robock 2018).

The ocean is expected to respond to volcanic eruptions in two fundamental ways. First, an immediate thermodynamic response results from aerosol scattering of solar radiation, which leads to sea surface temperature (SST)

[a] Additional affiliation: Center for Climate Physics, Institute for Basic Science, Busan, South Korea.

[b] Current affiliation: Department of Atmospheric and Oceanic Sciences, University of Colorado Boulder, Boulder, Colorado.

Corresponding author: Yassir A. Eddebbar, yeddebba@ucsd.edu

DOI: 10.1175/JCLI-D-18-0458.1

cooling (Rampino and Self 1982), reduced ocean heat content (Delworth et al. 2005; Stenchikov et al. 2009), and decreased thermosteric sea level (Gleckler et al. 2006). Second, a dynamical ocean response can result from volcanic perturbations of atmospheric and ocean temperature gradients, potentially influencing ocean circulation and projecting onto modes of natural climate variability (Zanchettin et al. 2012). Paleoproxies, for instance, indicate El Niño conditions follow major eruptions (Adams et al. 2003).

To explain this dynamical response, Mann et al. (2005) have invoked the ''ocean dynamical thermostat'' mechanism (Clement et al. 1996), whereby volcanic radiative forcing causes less cooling in the eastern equatorial Pacific than in the west due to buffering by upwelling of unperturbed thermocline waters in the east. This asymmetric cooling reduces the equatorial zonal SST gradient, thus weakening the easterlies and initiating Bjerknes feedbacks wherein decreased and shallower upwelling leads to further surface warming and the full development of El Niño (Emile-Geay et al. 2008). This effect is not uniform across models, however, with Ding et al. (2014) finding essentially no links between volcanoes and ENSO across CMIP5 models, whereas other models yield La Niña conditions following eruptions (McGregor and Timmermann 2011; Zanchettin et al. 2012), exposing key differences across models and observations.

More recently, model studies have shown that the tropical climate response to eruptions depends on the initial state of ENSO prior to eruption (Ohba et al. 2013; Pausata et al. 2016; Predybaylo et al. 2017) and may potentially be linked to volcanic cooling of the African continent through atmospheric teleconnections (Khodri et al. 2017). Other studies have shown that the ENSO response is sensitive to the timing and location of the eruption (Predybaylo et al. 2017; Stevenson et al. 2017; Liu et al. 2018) and that the ENSO response may be more readily detected in sea surface height (SSH) due to the confounding effects of volcanic cooling on surface temperature anomalies (Maher et al. 2015). A clear temporal evolution or mechanistic understanding of how volcanic eruptions affect the coupled ocean–atmosphere system, however, remains obscured by the freely evolving nature of ENSO regardless of external forcing.

Volcanic eruptions also trigger strong responses in ocean biogeochemistry. The otherwise persistent increase in atmospheric CO_2, for instance, stalled in the years following the June 1991 eruption of Pinatubo (Sarmiento 1993), driven by an uncertain combination of terrestrial and ocean carbon uptake (Frölicher et al. 2011, 2013; Segschneider et al. 2013). The role of volcanic eruptions in driving interannual-to-decadal variability in air–sea oxygen (O_2) exchange and interior dissolved O_2 ($[O_2]$) remains largely unexplored (Frölicher et al. 2009). Isolating these volcanic effects on air–sea heat, carbon, and oxygen exchange is thus critical to the detection and attribution of anthropogenic impacts in the ocean, such as warming, oxygen loss, and acidification (Bopp et al. 2013; Schmidtko et al. 2017; Ito et al. 2017; Long et al. 2016), and is highly relevant to discussions of decadal variability in the oceanic heat and carbon sinks in recent decades (Balmaseda et al. 2013; Landschützer et al. 2015). The magnitude and mechanisms driving the physical and biogeochemical ocean response to volcanoes, however, remain obscured by the confounding effects of internal variability and the lack of global ocean observations spanning major eruptions.

In models, discerning the volcanically forced ocean response in the presence of intrinsic climate variability has been hindered by the limited number of ensemble members in past studies (Frölicher et al. 2009, 2013; Ding et al. 2014). Multimodel ensemble studies (e.g., the CMIP5 archive), despite their large number of ensemble members, combine uncertainty due to model structure with internal variability, thereby limiting inferences regarding ''forced'' signals (Kay et al. 2015; McKinley et al. 2016; Long et al. 2016).

In this study, we focus instead on a Large Ensemble (LE) suite from a single climate model, the Community Earth System Model (CESM), forced with volcanic radiative perturbations (section 2). In the LE experiment, a large number of ensemble members from the same Earth system model were forced with identical external forcing from historical anthropogenic and volcanic emissions, but were initialized with unique small perturbations to the initial conditions (Deser et al. 2012; Kay et al. 2015). Modes of internal variability are effectively randomized across the ensemble within a decade, and averaging across a sufficiently large number of ensemble members isolates the externally forced response due to volcanic eruptions. We evaluate model differences by comparing results from a similar LE experiment using the Geophysical Fluid Dynamics Laboratory (GFDL) Earth System Model (ESM2M LE). We emphasize that we are primarily concerned in this study with isolating the externally forced ocean response to tropical eruptions irrespective of initial ENSO conditions or ''preconditioning'' during the eruption year, as the ocean response outside of the tropical Pacific may not be directly linked to ENSO. We do, however, examine the sensitivity of the ocean response to ENSO preconditioning in the context of comparing models and observations of the June 1991 Pinatubo eruptions, which coincided with the moderate El Niño conditions of 1991/92.

Specifically, we examine simulations of the recent major tropical eruptions of Agung (March 1963),

TABLE 1. Description of recent major volcanic eruptions examined in the CESM and ESM2M LE experiment. Volcanic intensities are based on the Ice-Core Volcanic Intensity Index of Gao et al. (2008). We also show the Volcanic Explosivity Index (VEI) of Simkin and Siebert (1994), and the Dust Veil Index (DVI) of Lamb (1983), as updated by Robock and Free (1996).

Volcanic eruption	Date	Location	Intensity (Pg)	VEI	DVI
Agung, Indonesia	Mar 1963	8°S, 115°E	17	4	800
El Chichón, Mexico	Apr 1982	17°N, 93°W	14	5	800
Pinatubo, Philippines	Jun 1991	15°N, 120°E	30	6	1000

El Chichón (April 1982), and Pinatubo (June 1991), given their relatively similar region of eruption (i.e., the tropics) listed in Table 1 and their relevance to observed ocean trends in recent decades. In section 3, we evaluate the global mean and spatial patterns of SST, heat, O_2, and CO_2 air–sea exchanges and budgets as indicators of the ocean's physical and biogeochemical state following tropical eruptions. In section 4, we evaluate similarities and differences across models and observations and evaluate the role of initial ENSO conditions during eruption on the ocean response. In section 5, we examine driving mechanisms, focusing on the June 1991 eruption of Pinatubo, the largest and best-observed eruption of the last 100 years. We conclude in section 6 with a summary and discussion of our results.

2. Methods

a. The Large Ensemble Experiment

The CESM LE configuration is run at the 1° × 1° nominal horizontal resolution of CESM version 1, which couples the Community Atmosphere Model version 5 (Hurrell et al. 2013) to the Parallel Ocean Program version 2 (Danabasoglu et al. 2012) and the Los Alamos Sea Ice Model version 4 (Hunke et al. 2008). Ocean biogeochemistry is also coupled in the ocean model and simulated using the Biogeochemical Elemental Cycling model (Moore et al. 2013). We evaluate 41 ensemble runs for physical variables, and 35 runs for biogeochemical fields for the period of 1950–2005. Ensemble runs were initialized from a 600-yr spinup model solution and were forced with identical prescribed CO_2 mixing ratio based on observations. Volcanic radiative forcing is incorporated in the CESM LE using the forcing dataset of Ammann et al. (2003). Here, stratospheric sulfate aerosol loading, characterized herein using aerosol optical depth (AOD) at 0.5 microns (500 nm), is based on total sulfates ejected from each eruption and the resulting sulfate aerosol temporal evolution and latitudinal distribution due to the seasonally dependent stratospheric transport. Initial conditions for each ensemble member were perturbed with a round-off level perturbation (10^{-14} K) to atmospheric surface temperatures, which randomizes modes of variability within a decade across ensembles. The LE mean is then evaluated for volcanic and anthropogenic forcing components.

For the ESM2M model, we analyze 30 ensemble members for the period of 1950–2005 for both physical and biogeochemical fields. Here, ensemble runs 2–30 are initialized with slightly different initial conditions by using snapshots from days 1–29 from ensemble run 1, as detailed in Rodgers et al. (2015). The ESM2M-LE configuration was based on the GFDL-ESM2M (Dunne et al. 2012, 2013) in its 1° × 1° nominal resolution, where the atmospheric model AM2 (Anderson et al. 2004) is coupled to the ocean component MOM4p1 (Griffies et al. 2009) and a model of ocean biogeochemistry, Tracers of Ocean Phytoplankton and Allometric Zooplankton version 2 (TOPAZ2; Dunne et al. 2010). The revised aerosol loading product of Sato et al. (1993), as introduced by Stenchikov et al. (1998, 2006), is used in the ESM2M LE, which results in a slightly lower AOD than obtained from Ammann et al. (2003). The different model components and volcanic forcing used in ESM2M LE versus CESM LE allow us to evaluate the impacts of model structure and choice of volcanic forcing on our results.

To isolate volcanic influence on the ocean carbon cycle from changes due to ocean uptake of anthropogenic CO_2, we examine variability in a ''natural'' or ''preindustrial'' ocean carbon tracer. This natural carbon tracer is exposed to a constant atmospheric CO_2 concentration of 284.7 ppm and reflects primarily changes in ocean carbon cycling due to climate perturbations (e.g., volcanic impacts), while radiative forcing and the contemporary carbon cycle (i.e., the sum of natural and anthropogenic components) are influenced by the rising historical anthropogenic emissions of CO_2. We also briefly evaluate volcanic effects on contemporary carbon in our comparison of CESM and ESM2M due to the lack of a natural carbon tracer in ESM2M, but focus our mechanistic and spatial analysis on the natural carbon cycle for clarity.

Monthly anomalies are calculated for all series by removing the long-term climatological seasonal cycle, based here on the 1950–2005 simulation period. To highlight volcanic signals in the spatial analysis and mechanism section, long-term trends due to anthropogenic warming

computed from the LE mean are removed through linear detrending. We note that our results are insensitive to the climatological period selection, as we obtain similar results when calculating anomalies based on climatologies obtained from a 100-yr control simulation with no volcanic or anthropogenic forcing, a 5-yr reference period prior to Pinatubo, or a 10-yr reference period prior to Agung. To characterize spatial anomalies following eruptions, we show annual mean anomalies in the years following the eruptions of Agung (March 1963), El Chichón (April 1982), and Pinatubo (June 1991), using July as the first month of each year to ensure symmetry around the peak of ENSO. We thus refer to the 12 months following the eruption date as year 0 [July(0)–June(0)], and subsequent years as year 1 [July(1)–June(1)], and year 2 [July(2)–June(2)]. Similarly, the seasonal evolution of atmospheric and oceanic conditions are presented as seasonally averaged anomalies following eruption, with SON(0), for instance, referring to the September–November period directly following the eruption, and SON(1) referring to the subsequent year (year 1). Statistical significance of volcanic anomalies in the LE mean is evaluated across the ensemble members at the 95% confidence level using a two-tailed Student's t test. Throughout the paper, a positive anomaly in the air–sea flux of heat, O_2, or CO_2 indicates anomalous flux out of the ocean, while a negative flux denotes ocean uptake.

b. Observations

Because of limited global continuous ocean observations for the events prior to the 1990s, we focus our model-to-observations comparison on the Pinatubo eruption. Specifically, we evaluate SST anomalies from the Hadley Centre Sea Ice and Sea Surface Temperature dataset (HadISST; Rayner et al. 2003) for the full 1950–2005 period comparison (Fig. 1a) but employ the shorter and higher-quality NOAA Reynolds product (Reynolds et al. 2002) for the Pinatubo eruption comparison (Fig. 5f). We compare the simulated net air–sea heat flux to the Liu et al. (2015) product, which employs a mass-adjusted energy divergence method, satellite measurements of top-of-atmosphere energy fluxes, and energy transport and atmospheric energy tendencies from an atmospheric reanalysis product (Allan et al. 2014).

We compare O_2 fluxes to estimates of air–sea O_2 exchange based on time series of atmospheric potential oxygen ($APO = O_2 + 1.1CO_2$), an atmospheric tracer based on measurements of atmospheric O_2 and CO_2 (Stephens et al. 1998), where 1.1 is the biospheric $-O_2$:CO_2 molar exchange ratio (Severinghaus 1995). Because of tight coupling of terrestrial O_2 and CO_2 exchange, APO is insensitive to terrestrial perturbations. On interannual time scales, APO is dominated by variability in air–sea O_2 fluxes, and thus constrains the oceanic O_2 response to volcanic eruptions. The globally integrated air–sea flux of APO ($F_{APO} = F_{O_2} + 1.1F_{CO_2}$) can be inferred from the observed global mean APO as

$$F_{APO} = M_{atm} X_{O_2} \frac{d\mathrm{APO}_{GLB}}{dt}, \quad (1)$$

where M_{atm} is the number of moles in the atmosphere (1.77×10^{20} mol) and X_{O_2} is the atmospheric mixing ratio of O_2 (0.2095), and APO_{GLB} is the mean APO anomaly calculated from La Jolla and Cape Grim stations, the only locations where observations began at

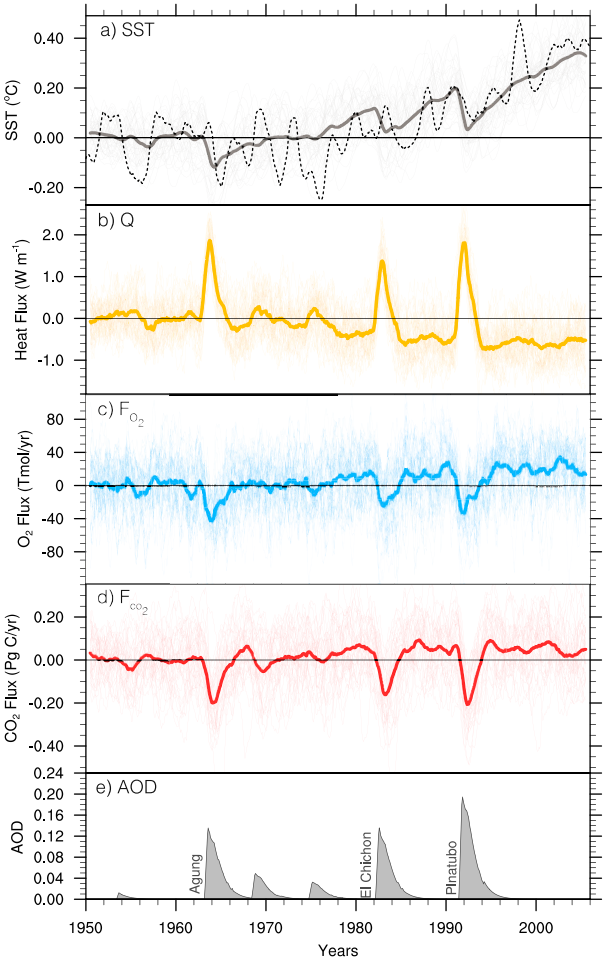

FIG. 1. CESM LE anomalies in (a) global mean SST, (b) globally integrated air–sea heat flux Q, (c) O_2 flux (F_{O_2}), (d) natural (i.e., preindustrial) CO_2 flux (F_{CO_2}), and (e) stratospheric aerosol optical depth (AOD) at 500 nm. Thin lines denote individual ensemble runs, while thick lines represent the LE mean. The dashed line in (a) represents the observed global mean SST based on the HadISST product (Rayner et al. 2003). Time series are seasonally detrended, smoothed with a 12-month running mean, and adjusted by subtracting the 1950–59 decadal mean anomaly as a reference period. Positive flux denotes flux out of the ocean.

least 6 months prior to the Pinatubo eruption (Keeling and Manning 2014). Owing to fast atmospheric mixing on interannual time scales, we expect these two stations to be adequate to resolve global air–sea APO flux changes. We compare the simulated carbon flux response to an observational product based on the Surface Ocean Carbon Atlas (SOCAT) dataset and a mixed layer scheme (Rödenbeck et al. 2014). To put the observed APO and CO_2 fluxes within the context of observed natural variability, we also evaluate fluxes from a hindcast simulation of CESM (Long et al. 2013), which simulates the expected ocean biogeochemical response (including APO and CO_2 fluxes) to observed atmospheric conditions.

In comparing the modeled and observed oceanic response to recent tropical eruptions (e.g., Pinatubo), which coincide with El Niño conditions during the eruption year (year 0), we take initial ENSO conditions during eruption year (i.e., preconditioning) into account by subsampling the ensemble for members with El Niño events during the eruption year. We use the El Niño definition of Trenberth (1997), and select members containing El Niño (EN) conditions during eruption year (9 members), whereby EN members must contain a Niño-3.4 index that exceeds 0.4°C for at least 6 consecutive months centered around DJF(0). We also subsample for neutral ($-0.4° \leq$ Niño-3.4 index ≤ 0.4°C) and La Niña conditions (Niño-3.4 index < -0.4°C) to evaluate the tropical Pacific climate response to eruptions following neutral and La Niña preconditioning as well.

3. Oceanic imprints of tropical eruptions

a. Global mean response

Figure 1 illustrates the simulated global mean SST and air–sea heat flux, and the globally integrated O_2 and CO_2 fluxes for CESM from 1950 to 2005, spanning the eruptions of Agung, El Chichón, and Pinatubo. The LE mean (bold lines) isolates clearly the effects of volcanic and anthropogenic forcing from internal noise, which dominates interannual-to-decadal variability in individual ensemble members (thin lines). The simulated multidecadal rise in global mean SST due to greenhouse gas forcing (≈0.4°C) from 1950 to 2005 is punctuated by sharp declines of about 0.1°–0.2°C in the year following the eruption. Similarly, the simulated long-term oceanic uptake of heat is disrupted by massive ocean heat loss events of about 2 W m^{-2} within 6–9 months following eruptions. Substantial oceanic uptake of O_2 up to 60 Tmol yr^{-1} is also simulated following volcanic events, acting in the opposite sense of the long-term O_2 outgassing trend due to anthropogenic warming. A volcanically forced response in "natural" CO_2 uptake of up to 0.3 Pg C yr^{-1} following eruptions is evident as well, opposing a weak long-term outgassing trend due to anthropogenic warming.

The impact of volcanic eruptions is also clearly evident in the globally averaged vertical profiles of potential temperature, $[O_2]$, and dissolved inorganic carbon (DIC) as shown in Fig. 2 for the CESM LE mean. The Agung, El Chichón, and Pinatubo eruptions act to significantly, although only temporarily, delay the advance of ocean warming, deoxygenation, and natural carbon loss in the upper ocean over the second half of the twentieth century. These volcanic impacts are particularly visible following the Agung eruption, when the anthropogenic warming effects are barely noticeable due to relatively weak anthropogenic forcing prior to 1970. Substantial cooling occurs after each event in the upper 100 m, propagating down to 500 m in depth through advective and diffusive mixing processes, and persists for more than a decade following the eruption. The $[O_2]$ anomalies show maxima below 100 m, suggesting a biological or dynamical response, and persist for about 7 years.

b. Spatial patterns

Figure 3 illustrates the spatial response in the CESM LE mean during the 3 years following the Pinatubo eruption. Ocean heat loss is strongest during the first year (year 0, 1–12 months) following the eruption with extensive heat flux anomalies and SST cooling over the tropics (Fig. 3a), as expected from the immediate effects of stratospheric aerosol scattering. SST cooling intensifies in the subsequent year (year 1) over most of the North and South Pacific, particularly over the northwest Pacific subpolar region where extensive ocean heat loss also occurs (Fig. 3b). El Niño–like tropical Pacific surface warming accompanies this cooling and is associated with significant ocean heat loss. In the following year (year 2), air–sea heat flux anomalies are largely subdued, while negative SST anomalies persist over the northwest subpolar and equatorial Pacific and the North Atlantic. We also note a positive Indian Ocean dipole–like SST pattern over the Indian basin (weak warm anomalies in western vs cold eastern SST anomalies) during year 1, and surface warming over the Southern Ocean that persists throughout the three years following eruption.

The simulated ocean biogeochemical response to Pinatubo is more regionally focused and varies less over time (right two panels of Fig. 3), with the peak response occurring during year 1 (13–24 months post eruption). Persistent and intense O_2 drawdown is evident over regions of mode, intermediate, and deep water formation such as the northwest Pacific, North Atlantic, and the Southern Ocean. Along the cold tongue in the equatorial

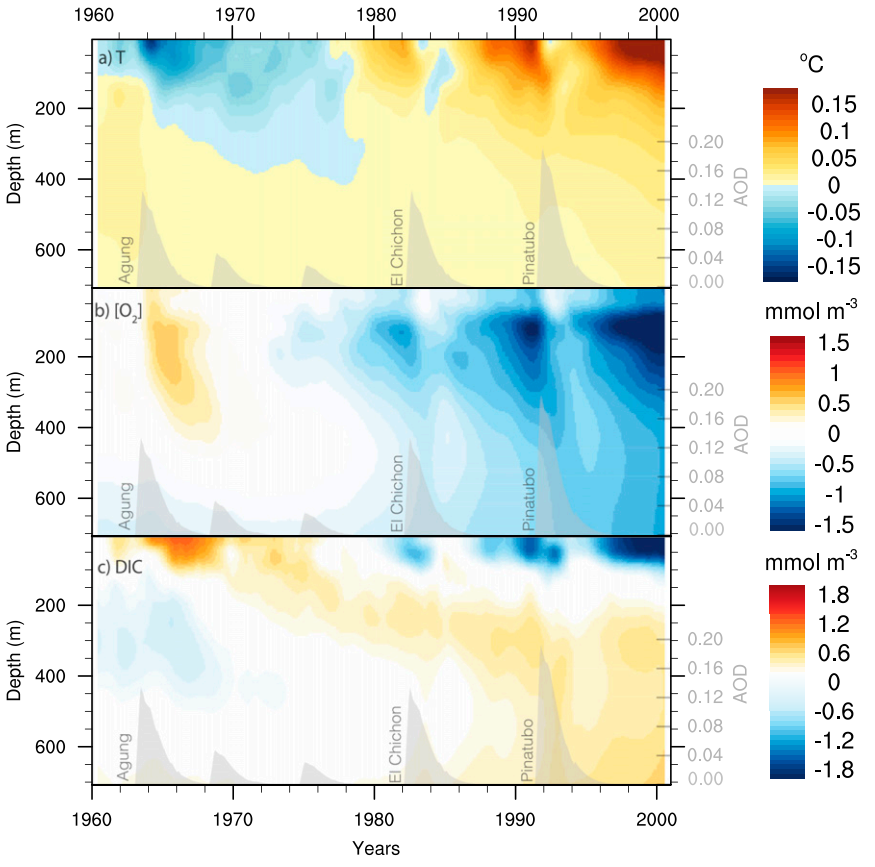

FIG. 2. Globally averaged vertical profile of CESM LE mean anomalies in (a) temperature, (b) $[O_2]$, and (c) "preindustrial" DIC. AOD (right axis) is also shown within each panel. Time series are seasonally detrended, smoothed with a 12-month running mean, and adjusted by subtracting the 1950–59 decadal mean anomaly as a reference period.

Pacific, anomalous O_2 outgassing acts to reduce the global oceanic O_2 uptake. CO_2 flux perturbations, on the other hand, are dominated by broad and intensive anomalous uptake (i.e., reduced outgassing) over the tropical Pacific, and are accompanied by weak anomalous outgassing at higher latitudes. The low-latitude ocean biogeochemical response to Pinatubo is reminiscent of El Niño impacts on air–sea CO_2 and O_2 exchanges that are typically dominated by equatorial ocean dynamics (Feely et al. 2002; Eddebbar et al. 2017).

Figures 4a–c show the simulated oceanic response during year 1 across all three eruptions. Similar to the global mean response shown in Fig. 1, the intensity of these patterns scales with the volcanic magnitude, with Pinatubo showing the most striking response. Similar patterns emerge for all variables across volcanic events in CESM, although the El Niño–like SST warming and equatorial O_2 outgassing do not emerge as clearly in Agung and El Chichón (below 95% statistical significance) as the CO_2 response, which exhibits a strong and statistically significant El Niño–like response (i.e., reduced tropical CO_2 outgassing) across all eruptions. Before we examine mechanisms driving the oceanic response to tropical eruptions, we first compare these CESM LE results to the ESM2M LE response, and evaluate the observations for these volcanic imprints.

4. Comparison of models and observations

a. *Comparison to the ESM2M LE*

A comparison of the CESM LE and ESM2M LE means in Figs. 5a–e shows a similar global ocean response despite differences in model structure and volcanic forcing. We note, however, slightly larger SST cooling, ocean heat loss, and O_2 uptake in ESM2M LE (Figs. 5a–c, dashed line), particularly following Agung even though AOD values used in the ESM2M simulations are actually lower. A slightly larger response to the long-term anthropogenic forcing is also found in ESM2M LE, suggesting a higher sensitivity to radiative forcing in this model. Because of the lack of a natural carbon

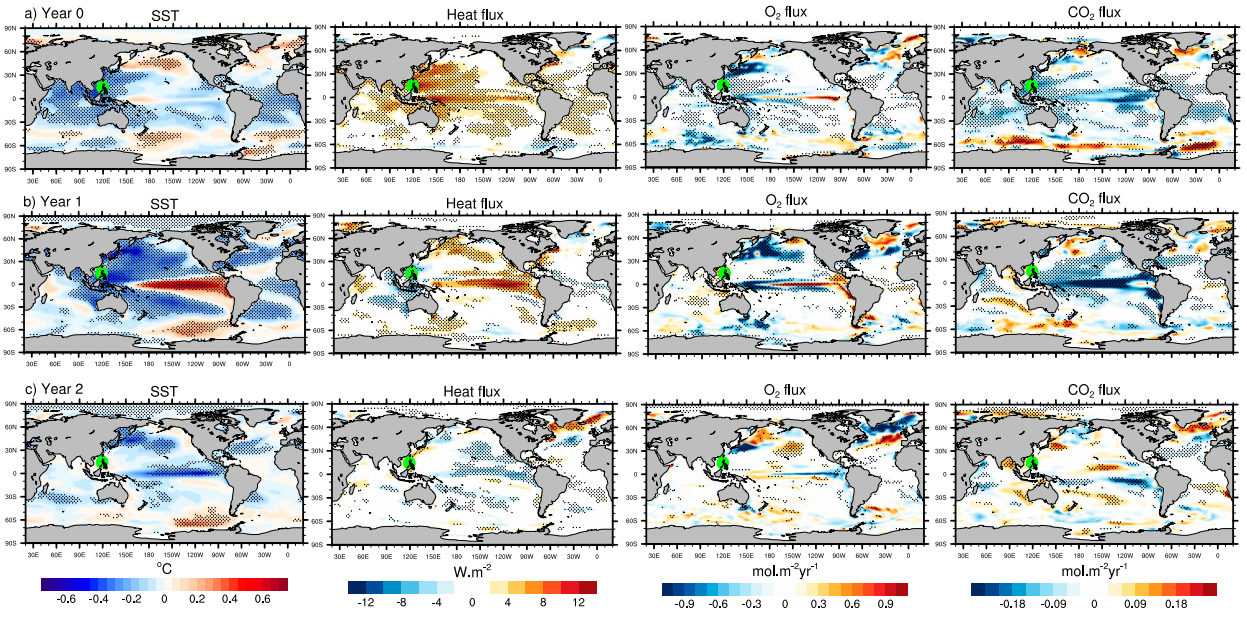

FIG. 3. Evolution of annual mean anomalies in SST, heat flux, F_{O_2}, and F_{CO_2} in the CESM LE mean during (a) 1–12 months [July(0)–June(0) or year 0], (b) 13–24 months [July(1)–June(1) or year 1], and (c) 25–36 months [July(2)–June(2) or year 2] after the June 1991 eruption of Pinatubo. Green triangle indicates eruption location. Anomalies are calculated by removing the seasonal cycle and linear detrending based on the 1950–2005 simulation period, and annually averaged over respective years (year 0, year 1, and year 2). Positive flux denotes flux out of the ocean. Stippling indicate statistically significant anomalies at the 95% confidence level.

tracer in the ESM2M LE, we compare the contemporary carbon flux response (i.e., anthropogenic and natural) in both models, and find noticeable interannual-to-decadal variability associated with volcanic events (Fig. 5d). Similar to natural carbon, contemporary carbon uptake is initially intensified after eruptions, followed by a multiyear recovery. The decade following the Pinatubo eruption shows an intriguing deceleration of ocean carbon uptake when compared to volcanically weak decades (i.e., 1970s), especially in ESM2M where recovery seems to overcompensate for the initial response.

The spatial patterns of the oceanic response are similar between the ESM2M LE and CESM LE means in year 1 following Pinatubo (Figs. 4c,f), including the El Niño–like response (i.e., anomalous warm SST, heat loss, uptake of CO_2, and outgassing of O_2) at low latitudes and the convective patterns (i.e., heat loss, outgassing of CO_2, and uptake of O_2) at higher latitudes. Following Pinatubo, more intensive SST cooling is evident in ESM2M over the northern subtropical Pacific as well as more confined warming in the equatorial Pacific region in ESM2M than in CESM. The El Chichón response is also similar between CESM and ESM2M (Figs. 4b,e), with generally weaker cooling globally and statistically insignificant weak tropical Pacific SST warming, and a strong El Niño–like CO_2 response. Finally, the Agung response in ESM2M differs from CESM with broader and more intense tropical SST cooling and O_2 uptake over the equatorial Pacific, but shows tropical Pacific CO_2 uptake and high-latitude O_2 uptake that are relatively similar to CESM (Figs. 4a,d). The unique SST response after Agung in ESM2M is likely related to the Southern Hemisphere–oriented AOD evolution of this specific eruption in this model (Maher et al. 2015) driving a Southern Hemisphere–like response that typically does not showcase an El Niño–like SST pattern (Liu et al. 2018). Overall, with the exception of the Agung response in ESM2M, the simulated oceanic patterns shown in Fig. 4 show a relatively consistent ocean response to tropical eruptions across models and eruptions, suggesting relatively similar governing mechanisms at play.

b. *Comparison to observations*

Given Pinatubo's larger forcing, its enhanced observational coverage, and its clear and similar signature in both CESM LE and ESM2M LE means, we focus our model–observation comparison on the CESM LE response after Pinatubo (Figs. 5f–i). Similar to an individual ensemble member, volcanic imprints in observations (black lines) are embedded within the climate system's internal variability, which we characterize here using the 2σ spread across ensemble members (shading).

Observed global SST cooling and ocean heat loss following the Pinatubo eruption are in general agreement in

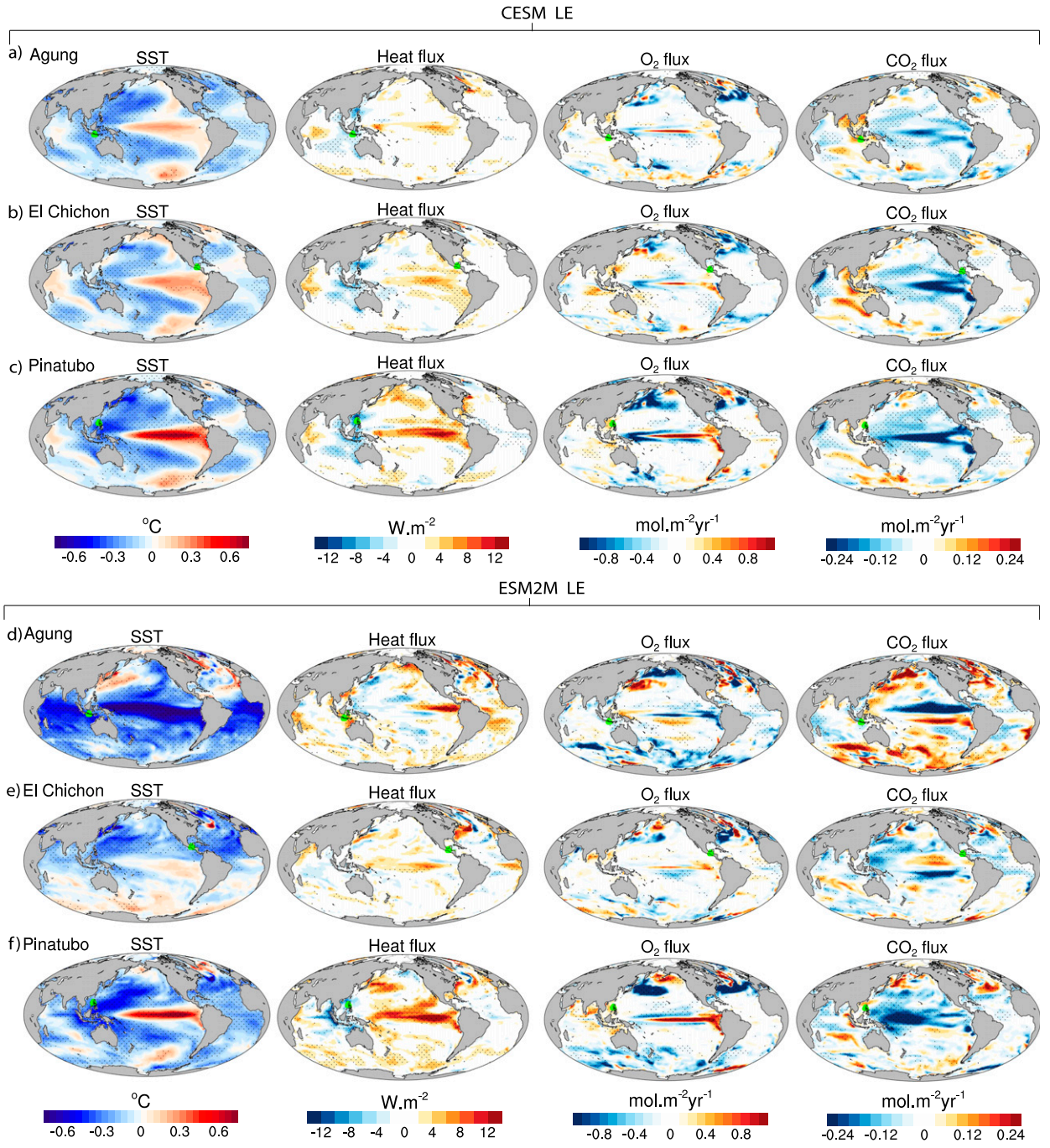

FIG. 4. Anomalies in SST, heat flux, F_{O_2}, and F_{CO_2} in the CESM LE mean for the first year [July(1)–June(1)] following the eruptions of (a) Agung, (b) El Chichón, and (c) Pinatubo. (d)–(f) As in (a)–(c), but for the ESM2M LE mean. Eruption locations are shown in green triangles. Anomalies are calculated by removing the seasonal cycle and linear detrending based on the 1950–2005 simulation period, and annually averaged over year 1. Stippling indicates statistically significant anomalies at the 95% confidence level. Positive flux denotes flux out of the ocean.

phase and magnitude with the CESM LE mean response (Figs. 5f,g). A potentially longer heat flux recovery emerges in the observations-based product compared to the CESM LE mean response, although this behavior is well within the 2σ spread and may be influenced by internal variability. Global SST cooling is observed despite the occurrence of an El Niño event during the eruption year, which typically tends to warm global

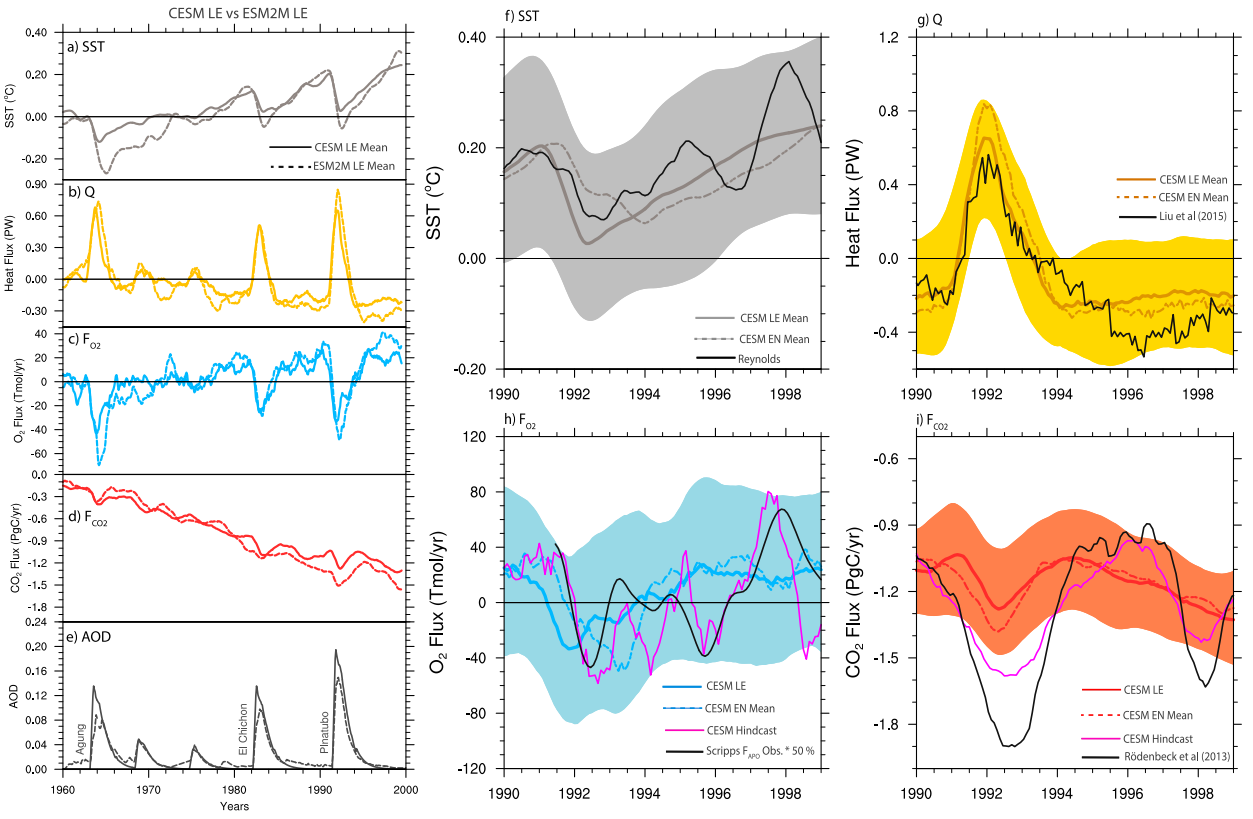

FIG. 5. Comparison of CESM LE mean (continuous line) and the ESM2M LE mean (dashed line) in (a) global mean SST, (b) air–sea heat flux (Q), (c) O_2 flux, (d) CO_2 flux, and (e) stratospheric aerosol optical depth at 500 nm. (right panel) A comparison of CESM LE mean to observations-based estimates during the Pinatubo period for (f) global mean SST from the Reynolds et al. (2002) product (black) and simulated LE mean SST (gray line), (g) air–sea heat flux from the Liu et al. (2015) product and simulated heat flux (orange), (h) O_2 flux (simulated LE in blue) vs the observations-based flux of APO scaled down by 50% (black) and hindcast simulation flux of O_2 (purple), and (i) CO_2 flux (LE simulation in red) vs observations-based (Rödenbeck et al. 2014; black) and hindcast simulation (purple). The mean of CESM ensemble members with an El Niño event during eruption year are shown in dashed lines in (f)–(i). The observations-based APO flux is normalized (by 50%) to visualize phase comparison with simulated O_2 variability in the hindcast simulation. Series are seasonally detrended and smoothed with a 12-month running mean. Anomalies in observations are aligned with models using the CESM LE 1990/91 mean as a reference period. Color shadings indicate 2σ across ensemble members. Positive flux denotes flux out of the ocean.

SST, acting to delay the global cooling driven by negative radiative forcing. The delayed cooling effects of coincident El Niño events on observed global mean SST (dashed black line in Fig. 1a) is most apparent during the eruption year (year 0) of El Chichón and Agung (Fig. 1a) and has been shown to contribute significantly to the mismatch between simulated and observed global mean surface air temperature changes following these eruptions (Santer et al. 2014; Lehner et al. 2016). A subsampled set of El Niño ensemble members (i.e., members whose eruption year coincides with an El Niño event) shows this effect after Pinatubo more visibly, with slightly more delayed cooling in the El Niño (EN) ensemble mean (dashed gray line in Fig. 5f).

The simulated ENSO response to tropical eruptions has been suggested to depend in part on ENSO conditions during the eruption year (Predybaylo et al. 2017). To take this effect into account in our comparison to the observed Niño-3.4 index following Pinatubo, which coincided with a moderate El Niño event during eruption year, we stratify the ensemble members by ENSO conditions during eruption year, as described in the methods section. Figure 6 illustrates the sensitivity of the volcanic impacts on tropical Pacific climate in year 1 to ENSO preconditioning during year 0 of Pinatubo, whereby warm anomalies arise following El Niño and neutral preconditioning, while no major anomalies or perhaps an earlier termination of La Niña follow La Niña preconditioning, in general agreement with previous work by Ohba et al. (2013) and Predybaylo et al. (2017). Figure 6b further shows the observed Niño-3.4 index response (extended weak El Niño conditions in year 1; gray line) is in relative agreement with the EN ensemble mean response (red bold line showing

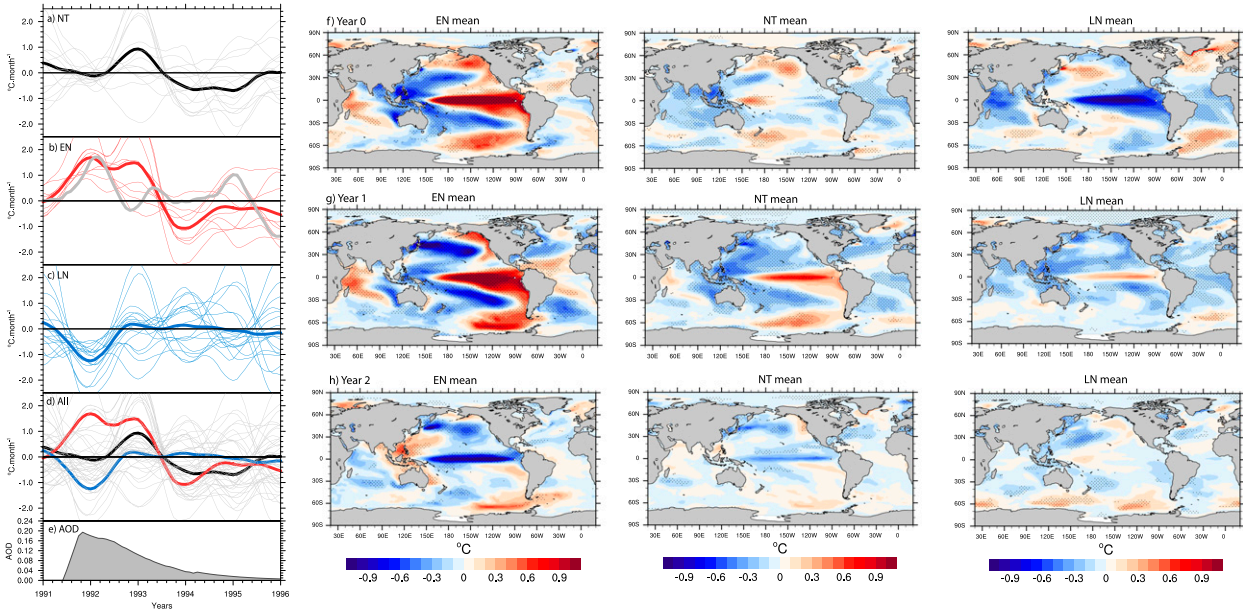

FIG. 6. Niño-3.4 index time series in CESM ensemble members coinciding with (a) neutral (NT in black; 16 members), (b) El Niño (EN in red; 9 members) and observations (gray) based on the Reynolds et al. (2002) product, and (c) La Niña (LN in blue; 16 members) conditions during the Pinatubo eruption year. Bold lines indicate the ENSO-phase ensemble mean while thin lines denote specific ensemble members. (a)–(c) are combined in (d) for visual comparison, while (e) shows AOD used in CESM. (f)–(h) The evolution of annual mean spatial anomalies in SST in the CESM ensembles means, categorized similarly by ENSO phase, with (left) El Niño, (middle) neutral, and (right) La Niña ensemble means during (f) year 0, (g) year 1, and (h) year 2 after the June 1991 eruption of Pinatubo. Anomalies are calculated by removing the seasonal cycle and linear detrending based on the 1950–2005 simulation period, and annually averaged over respective years (year 0, year 1, and year 2). Stippling indicates statistically significant anomalies at the 95% confidence level.

extended El Niño conditions through year 1), suggesting potentially detectable fingerprints of the Pinatubo effect on tropical Pacific climate in the observations.

Next, we compare the simulated O_2 flux response to APO flux anomalies inferred from atmospheric measurements of O_2 and CO_2 (dashed black line in Fig. 5i). APO variability on interannual time scales is largely dominated by changes in air–sea O_2 flux (Eddebbar et al. 2017), and thus APO can be used to compare models and observations of air–sea O_2 flux anomalies following eruptions. A noticeable and delayed APO drawdown is observed after Pinatubo followed by large variability, which is generally in line with the expected volcanic response and the low signal-to-noise found in CESM LE (Fig. 1c). A hindcast simulation of CESM (purple line in Fig. 5h), which independently simulates the ocean response to ''observed'' atmospheric forcing, shows a similarly delayed O_2 drawdown, recovery, and enhanced variability that drive the APO fluxes, lending further confidence in the observed APO features. Similar to the simulated SST response, subsampling for the EN members (dashed blue) yields delayed air–sea O_2 uptake and thus better phase agreement with observations, underscoring the importance of ENSO preconditioning in modulating the global biogeochemical ocean response as well. We note that the ''observed'' APO flux has been normalized by 50% to visualize phase comparison with the CESM LE and hindcast simulation and that the actual magnitude of the APO anomaly following Pinatubo exceeds 170 Tmol yr^{-1}, which is well outside the 2σ ensemble spread.

The SOCAT-based CO_2 flux anomaly (dashed black line in Fig. 5h) also shows vigorous ocean carbon uptake following Pinatubo that is in phase with the CESM LE and hindcast results (red and purple lines respectively). Subsampling for the EN members (dashed red) yields slightly better agreement with observations, which remain much larger in comparison with both simulations. This observed CO_2 uptake represents the largest flux anomaly during the 1990s, which includes the reduced outgassing associated with the 1997/98 El Niño event (Feely et al. 2002), and is well outside the 2σ spread, independently suggesting a larger biogeochemical sensitivity to eruptions in observations.

5. Mechanisms

The relatively consistent ocean response to tropical eruptions in both models and observations indicates a

distinct and robust mechanism at play. The emergence of an El Niño–like response in the models is especially of interest, given its central role in modulating the global SST, heat, and CO_2 flux anomalies and buffering the global O_2 uptake. In this section, we examine governing processes driving the simulated physical and biogeochemical ocean response, focusing again on the large and well-observed Pinatubo eruption.

a. ENSO response

The time evolution of anomalies in equatorial Pacific (2°N–2°S) SST, mixed layer depth, SSH, and zonal wind stress following Pinatubo is shown for the CESM and ESM2M LE means in Fig. 7. We note the close-to-neutral conditions that prevail in SST, SSH, and zonal wind stress (Figs. 7b–e) prior to eruption in both models, supporting the assumption of neutralized ENSO phase in the LE mean calculation outside of eruption events, and the emergence of an externally forced ENSO response following eruption. In both models, initial cooling in the eastern and central Pacific directly follows eruption (year 0), although this SST cooling in CESM is relatively weak and statistically insignificant, while ESM2M shows stronger cooling accompanied by slightly enhanced easterlies and weak negative SSH anomalies. This cooling is quickly followed in both models by considerable warming (≈1°C) 12 months later (year 1), peaking in early winter in CESM and late winter in ESM2M, before cooling takes over again in subsequent years (year 2 and 3). This SST warming is preceded in both models by anomalies in zonal wind stress, SSH (Figs. 7c,e), and mixed layer depth (line contours in Figs. 7b,d) that propagate from the western and central equatorial Pacific to the eastern equatorial Pacific. We also note subsequent weak La Niña–like conditions that prevail in years 2 and 3 across ENSO indicators in both models. Figure 7 thus illustrates a temporally rich and complex equatorial ENSO response that is relatively consistent between models.

To understand the warming response in the eastern and central equatorial Pacific, we examine the mixed layer heat budget over the equatorial Niño-3.4 region in the CESM LE and ESM2M LE means, following Huang et al. (2010) as

$$\frac{\partial T}{\partial t} = \frac{Q}{\rho C_p H} - w_e \frac{(T - T_H)}{H} - u\frac{\partial T}{\partial x} - v\frac{\partial T}{\partial y} - D, \qquad (2)$$

where T represents the mixed layer mean temperature and T_H represents temperature at the base of the mixed layer, Q represents the net air–sea heat flux going into the mixed layer, ρ is seawater density, C_p is seawater heat capacity, H is the mixed layer depth, u and v represent zonal and meridional current velocities respectively averaged over the mixed layer, D represents residual contributions from diffusive mixing and mesoscale processes, and w_e is the entrainment velocity, calculated as

$$w_e = \frac{\partial \mathrm{H}}{\partial t} + u_h\frac{\partial H}{\partial x} + v_h\frac{\partial H}{\partial y} + w_h, \qquad (3)$$

where u_h, v_h, and w_h represent velocities at the base of the mixed layer. The anomaly in the heating tendency $\partial T'/\partial t$ is dominated by a few terms, and we thus rewrite the anomalies in the mixed layer heat budget equation as follows:

$$\frac{\partial T'}{\partial t} \approx \frac{Q'}{\rho C_p H} - \overline{w_e}\frac{(T - T_H)'}{H} - w_e'\frac{\overline{(T - T_H)}}{H} - u'\frac{\overline{\partial T}}{\partial x}, \qquad (4)$$

where a prime notation represents an anomaly and a bar notation indicates the long-term mean.

For visual clarity, only dominant terms driving $\partial T'/\partial t$ (black line) are shown in Fig. 7f (for CESM) and Fig. 7g (for ESM2M). In CESM, the mixed layer heating tendency (black line) is driven in the 12 months following eruption primarily by the thermocline feedback term $[-\overline{w_e}(T - T_H)'/H$; dotted dark blue line], which represents the upwelling by the mean entrainment velocity of anomalies in the vertical temperature contrast at the base of the mixed layer. As illustrated later, this vertical temperature contrast is driven by anomalies in T_H. Warming of the mixed layer in CESM is later reinforced and eventually dominated by the Ekman upwelling feedback term $[-w_e'\overline{(T - T_H)}/H$; dashed cyan line], which represents the reduced upwelling of cold thermocline waters. The zonal advective term $(-u'\overline{\partial T}/\partial x)$ also contributes to warming in this model, albeit to a much lesser extent. Similar to CESM, the initial warming response in ESM2M is dominated by the thermocline feedback term, but is reinforced instead by the zonal advective term, while the Ekman upwelling feedback term plays a minor role in this model (Fig. 7g). Anomalies associated with meridional advection $(-v\partial T/\partial y)$ are much smaller in both models and are not shown here for clarity. In addition to initiating the warming response in both models, the thermocline feedback term $[-\overline{w}(T - T_H)'/H]$ also drives the termination of the warming event and subsequent cooling. The important role of the thermocline feedback in the initiation of the warming response and the lagged contribution of the Ekman upwelling and zonal advective feedbacks reflect two possible and distinct mechanisms:

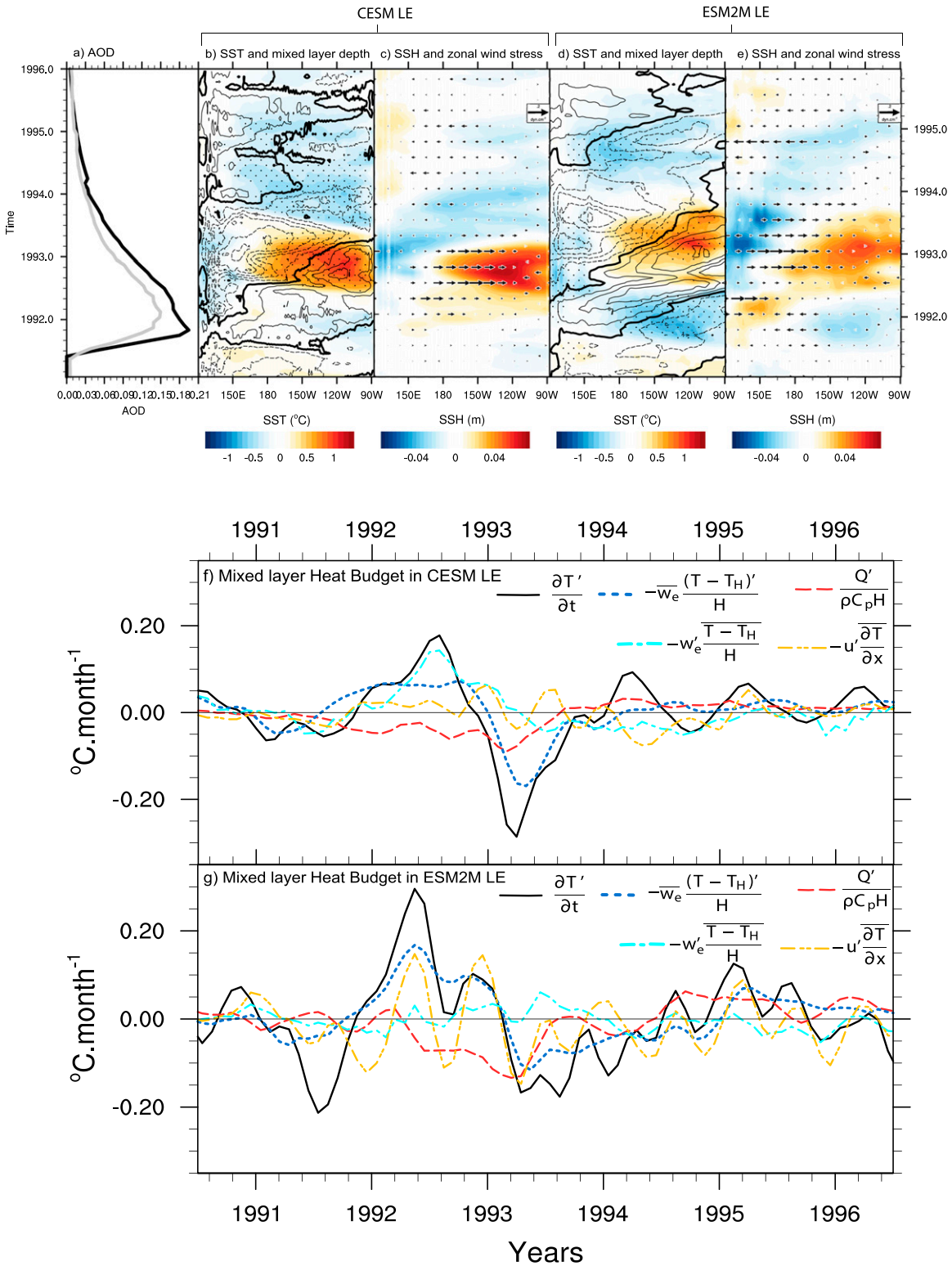

FIG. 7. (a) Aerosol optical depth (AOD) for CESM (black) and ESM2M (gray), and Hovmöller diagram of CESM LE mean anomalies in (b) SST (color shading) and mixed layer depth (contour) and (c) sea surface height (SSH, color shading) and zonal wind stress (arrow) averaged over the equatorial Pacific band (2°N–2°S) following Pinatubo. (d),(e) As in (b),(c), respectively, but for ESM2M LE. (f) Mixed layer heat budget from the CESM LE mean over the Niño-3.4 equatorial region (2°N–2°S) showing only dominant terms for visual clarity, including heating tendency (black), thermocline feedback term (dotted dark blue), Ekman upwelling feedback (cyan), heat flux (dashed

1) upwelling of unperturbed subsurface waters weaken surface cooling, thereby reducing the zonal SST gradient (i.e., ocean dynamical thermostat mechanism), and initiating Bjerknes feedbacks that lead to El Niño; or
2) upwelling of warm subsurface anomalies (e.g., due to deepening of the thermocline by internal waves) warms SST in the east and promotes El Niño development through initiation of Bjerknes feedbacks.

To evaluate which mechanism is at play, Fig. 8 illustrates the seasonal evolution in the CESM and ESM2M LE mean of precipitation, sea level pressure, surface air temperature, wind anomalies, and equatorial ocean temperature anomalies at depth following Pinatubo, showing largely neutral condition in the initial season [JJA(0)]. In contrast to what is expected from the dynamical thermostat mechanism (Mann et al. 2005; Emile-Geay et al. 2008), the equatorial Pacific zonal SST gradient actually increases in fall [SON(0)] and winter [DJF(0)] following eruption through surface cooling in the east (Figs. 8b,e, upper three panels). This SST cooling overlays an increasingly large subsurface warming in the eastern and central Pacific associated with a gradual deepening of the thermocline (Figs. 8c,f). No significant surface wind anomalies in the eastern Pacific accompany this initial subsurface warming, indicating remote forcing via the ocean from the western Pacific, where persistent westerly wind anomalies drive the eastward propagation of downwelling Kelvin waves from fall [SON(0)] through spring [MAM(0)] following the eruption in CESM. This subsurface warming feeds eastern and central equatorial Pacific SST warming through climatological equatorial upwelling, which reduces the zonal SST gradient and significantly weakens the Walker circulation during the subsequent summer [JJA (+1)] and fall [SON (+1)], promoting the full development of El Niño conditions by winter [DJF(+1)] of the following year in CESM. Note the lag of 2–3 months in the ESM2M anomalies in Figs. 8d–f in the westerly winds, SLP, precipitation, SST, and other ENSO phase indicators (e.g., SSH and zonal wind stress; Figs. 7c,e), likely due to the delayed peak in AOD used in this model (gray vs black line in Fig. 7a). Figure 8 thus suggests that the initial surface wind anomalies over the western Pacific play a more prominent role in initiating the El Niño response than direct buffering effects described in the ocean dynamical thermostat by Mann et al. (2005).

These initial and persistent westerly wind anomalies are associated with dry and cold surface air temperatures over the Maritime Continent (Figs. 8a,b,d,e). An expected consequence of volcanic radiative forcing is faster cooling over land relative to the ocean (Ohba et al. 2013) due to lower heat capacity and distinct surface feedbacks on land, resulting in an anomalous land–ocean temperature gradient between the Maritime Continent and the western Pacific. The cooling over the Maritime Continent likely originates from the advection of cold continental air from the much colder Asian continent by the equatorward climatological winds during the peak AOD period [SON(0)–DJF(0) in CESM and DJF(0)–MAM(0) in ESM2M] and the presence of large island landmasses in this region. Following the Gill model, which predicts an eastward propagation of easterly wind-inducing atmospheric Kelvin waves following heating of equatorial convective regions (Gill 1980), the intense volcanic cooling of the Maritime Continent suppresses convection and induces anomalous divergence and eastward atmospheric Kelvin wave propagation of westerly wind anomalies over the western Pacific. These persistent westerly wind anomalies continue to excite oceanic downwelling Kelvin waves throughout the eruption year (year 0) until the Bjerknes feedbacks take over [JJA(1) onward], when surface warming and a weakened walker circulation dominate, along with increased rainfall over most of the equatorial Pacific and a southward migration of the intertropical convergence zone (ITCZ).

b. *Ocean heat response*

While oceanic heat loss is expected following eruptions due to reduced shortwave radiation, it remains unclear where heat loss occurs regionally and how feedbacks in the coupled ocean–atmosphere system (e.g., clouds) amplify or dampen the net change in air–sea heat flux. We first examine the contribution of different components of the net air–sea heat flux (Q_T) in the CESM LE mean, which is calculated as

$$Q_T = Q_{\mathrm{SW}} + Q_{\mathrm{LW}} + Q_{\mathrm{SH}} + Q_{\mathrm{LH}}, \tag{5}$$

where Q_{SW} and Q_{LW} represent shortwave and longwave radiative fluxes, respectively, and Q_{LH} and Q_{SH} represent turbulent latent heat and sensible heat fluxes respectively. Latent heat fluxes are driven by two distinct

←

red), and zonal advective term (orange dashed). (g) As in (f), but for ESM2M LE. Mixed layer heat budget terms are smoothed with a 3-month running mean. Mixed layer anomalies are contoured every 3 m. 20°C isotherm depth is used to represent mixed layer depths for ESM2M LE. The annual cycle and the long-term linear trend are removed in the calculation of anomalies. Stippling indicates significance at the 95% confidence level.

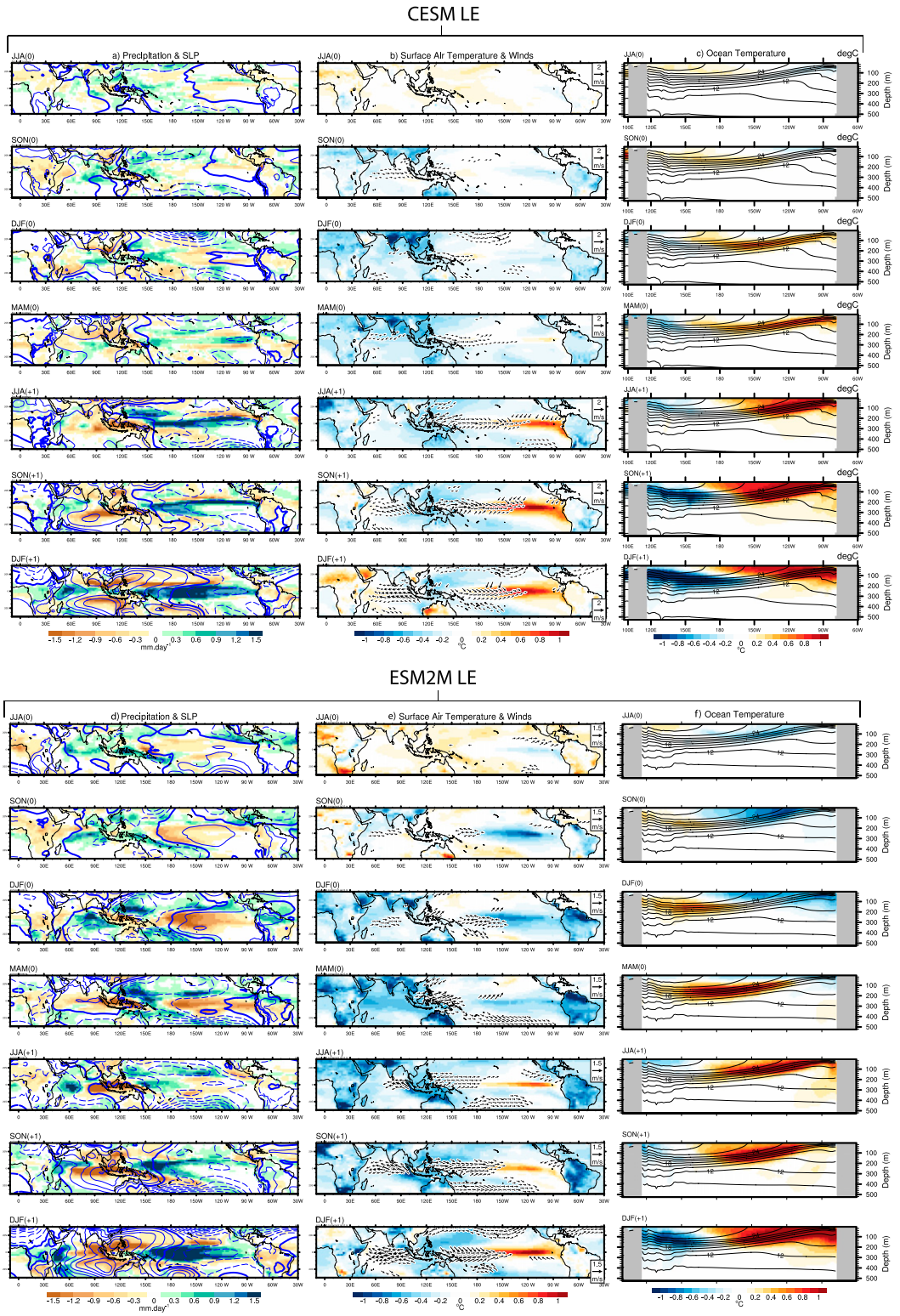

FIG. 8. Seasonal evolution of CESM LE mean anomalies following the eruption of Pinatubo in (a) rainfall and SLP, (b) surface air temperatures and winds, and (c) ocean temperatures in longitude vs depth averaged over the equatorial Pacific sector (2°N–2°S). (d)–(f) As in (a)–(c), but for ESM2M. Blue contours in (a) and (d) show SLP anomalies contoured every 0.2 hPa. Vectors show wind anomalies with 2 m s^{-1} reference wind in upper right box; wind anomalies weaker than 0.5 m s^{-1} are omitted for visual clarity. Black contours in (c) and (d) show climatological mean ocean temperature averaged over 2°N–2°S, contoured every 2°C.

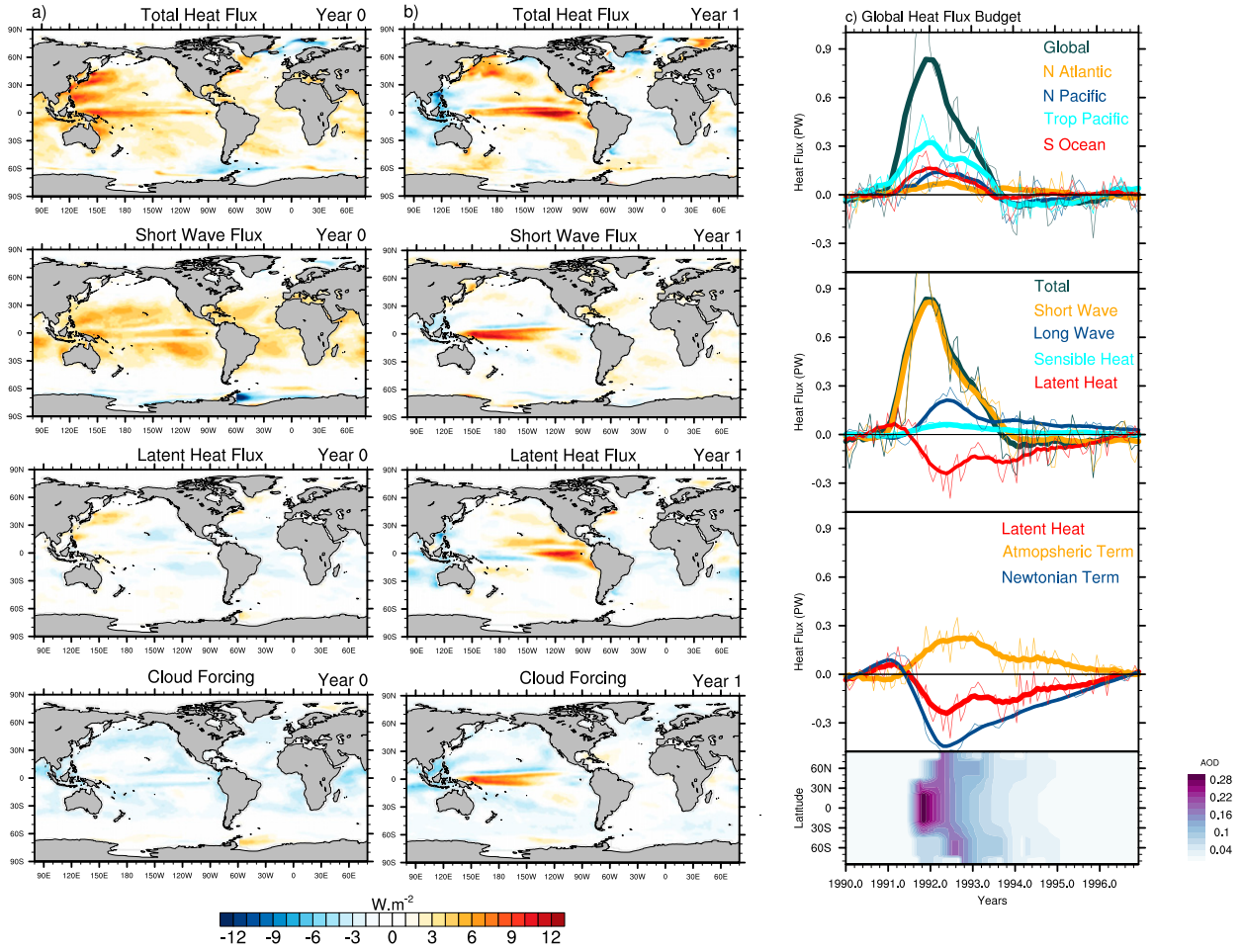

FIG. 9. CESM LE mean anomalies in total heat, shortwave, latent heat fluxes, and cloud forcing (a) during the Pinatubo eruption year (0–11 months post eruption on June 1991), and (b) a year after eruption (12–23 months post eruption). (c) The CESM LE mean globally integrated heat flux budget, decomposed by region (top) and by flux component (second from top) including shortwave, longwave, sensible, and latent heat fluxes. Third panel shows latent heat fluxes decomposed into atmospheric and Newtonian terms. Bottom panel shows latitudinal distribution of AOD at 500 nm. Spatial anomalies are calculated as annual mean anomalies during the two different years after eruption, with long-term linear trend removed. Thin lines indicate unfiltered series, while bold lines show 12-month running means. Positive anomalies denote flux out of the ocean.

processes: a Newtonian term (Q_{NT}), that is, the ocean's SST damping response (Xie et al. 2010), and an atmospheric term (Q_{ATM}) due to changes in surface humidity, winds, and other atmospheric properties. We isolate contributions from Q_{NT} following (Xie et al. 2010) as

$$Q_{NT} = \frac{L}{R_v T^2} \overline{Q_{LH}} T', \tag{6}$$

where L is the latent heat of evaporation, R_v is the water vapor gas constant, $\overline{Q_{LH}}$ represents the mean latent heat flux, and T' is the SST anomaly, and calculate Q_{ATM} as a residual ($Q_{ATM} = Q_{LH} - Q_{NT}$).

The initial heat flux response (year 0) is dominated by shortwave anomalies over the tropics (Fig. 9a), as expected due to the immediate and direct effects of aerosol scattering following a tropical eruption. However, the anomalies in Q_{SW} are not longitudinally uniform as expected from zonally uniform volcanic forcing, but are modified regionally by a widespread decrease in cloud radiative forcing due to variations in cloud cover.

The subsequent response (year 1) involves a more subtle balance between heat flux components (Figs. 9b,c). The term Q_{SW} still dominates the total response despite a significantly diminished tropical AOD. The Q_{SW} anomalies are localized over the equatorial Pacific region and are driven largely by enhanced cloud albedo due to El Niño–related shifts in convection (Fig. 8a). This heat loss is reinforced globally by widespread anomalies in Q_{LW} and to a smaller extent by Q_{SH} anomalies over the

north subpolar Pacific (not shown) and Q_{LH} anomalies in the eastern Pacific (Fig. 9b). Globally, Q_{LH} anomalies act to weaken the net ocean heat loss through the buffering effects of Q_{NT} (Fig. 9c) as SSTs cool, analogously to the ocean response to anthropogenic forcing (Xie et al. 2010). Figure 9 thus shows that a larger and longer ocean heat loss is simulated following an eruption than is expected from the reduced shortwave irradiance effects of volcanic aerosols alone, due to delayed feedbacks in the ocean–atmosphere system.

c. Oxygen response

The simultaneous global uptake of O_2 and CO_2 shown in the CESM LE mean in Fig. 1 could at face value be interpreted in the context of thermally induced fluxes as the dominant drivers of the O_2 and CO_2 responses, since cooling would increase solubility and drive influx in both gases. However, the spatial patterns of O_2 and CO_2 uptake are negatively correlated (Fig. 3), indicating a combination of ''biodynamical'' processes that impact exchanges between surface and subsurface waters (mixing and upwelling of low-O_2, carbon-rich waters) as playing a prominent role. We decompose the contribution of these effects in the CESM LE mean as

$$F_{O_2} = F_{Therm} + F_{BioDyn}, \tag{7}$$

where F_{Therm}, the thermal component of O_2 flux, is calculated following Keeling et al. (1993) as

$$F_{Therm} = \frac{\partial O_2^{sol}}{\partial T}\frac{Q_T}{\rho C_p}, \tag{8}$$

where O_2^{sol} represents surface O_2 solubility, Q_T is the net air–sea heat flux, ρ is sea water density, and C_p is seawater heat capacity. The term F_{BioDyn}, the O_2 flux component due to biological and dynamical processes, is computed as a residual. Spatial anomalies of each of these components from the CESM LE mean are shown in Figs. 10a–c, while their global integrals are shown in Fig. 10g.

Figure 10g shows that thermal and ''biodynamical'' effects reinforce each other and contribute nearly equally to the global response, though the F_{BioDyn} response persists longer. Whereas the global F_{Therm} response is the sum of relatively uniform but weaker spatial anomalies, the F_{BioDyn} response is a net balance of intense O_2 uptake at high latitudes and anomalous outgassing along the equatorial Pacific (Figs. 10b,c). This anomalous O_2 outgassing reflects the suppression of climatological ocean O_2 uptake along the cold tongue due to ENSO-related weakening of vertical transport of O_2-depleted waters by reduced upwelling rates and deepening of thermocline as illustrated in Fig. 8c.

Most of the simulated global O_2 uptake is driven by higher latitudes, with pronounced uptake in the North Pacific and the Southern Ocean (Fig. 10f). At higher latitudes, the F_{BioDyn} response is associated with intense surface cooling and large sensible heat and carbon fluxes to the atmosphere (Fig. 3), indicating vigorous convection and upwelling due to weakened stratification during anomalously cool winter seasons following eruptions. These ventilation events lead to significant O_2 uptake and introduction of new $[O_2]$ into the subtropical thermocline through mode and intermediate water mass formation, as shown by the depth-integrated $[O_2]$ anomalies and vertical profile of zonally averaged $[O_2]$ (Figs. 10d,e). Over the tropical Pacific, a strong zonal dipole in $[O_2]$ anomalies emerges due to ENSO-related isopycnal heaving and contraction of the eastern tropical Pacific oxygen minimum zone following eruption (Fig. 10d). Figure 10 describes yet another complex ocean response to tropical eruptions, whereby thermally driven O_2 influx and intensified convection and ventilation of interior waters drive substantial O_2 drawdown that is partially compensated in the global integral by the opposing effects of the El Niño response at lower latitudes.

d. Carbon response

In contrast to the O_2 flux response described above, the oceanic CO_2 uptake in CESM LE occurs primarily in the tropical Pacific, dominating over small outgassing anomalies at high latitudes (Figs. 11a,d). Various processes influence the air–sea exchange of CO_2 flux, which is calculated in the models following Wanninkhof (1992) as $F_{CO_2} = K\alpha\Delta pCO_2$, where K is the gas exchange piston velocity (a function of wind, ice fraction, and the Schmidt number), α is solubility, and ΔpCO_2 is the atmospheric–ocean difference in the partial pressure of CO_2. We use a linear Taylor expansion to separate the effects of gas piston velocity due to changes in winds and sea ice fraction versus changes in ΔpCO_2, following Long et al. (2013) as

$$F'_{CO_2} = \overline{K}(\alpha\Delta pCO_2)' + K'\overline{(\alpha\Delta pCO_2)} + \left[K'(\alpha\Delta pCO_2)' - \overline{K'(\alpha\Delta pCO_2)'}\right]. \tag{9}$$

Figure 11a shows that $\alpha\Delta pCO_2$ drives most of the CO_2 flux anomaly in the CESM LE mean and that reduced piston velocity, due to weakened easterlies (Fig. 8b), reinforces those changes in the central equatorial Pacific. We thus examine the contribution of different processes driving the surface ocean pCO_2 anomaly in CESM LE, including changes in surface temperature (T), DIC,

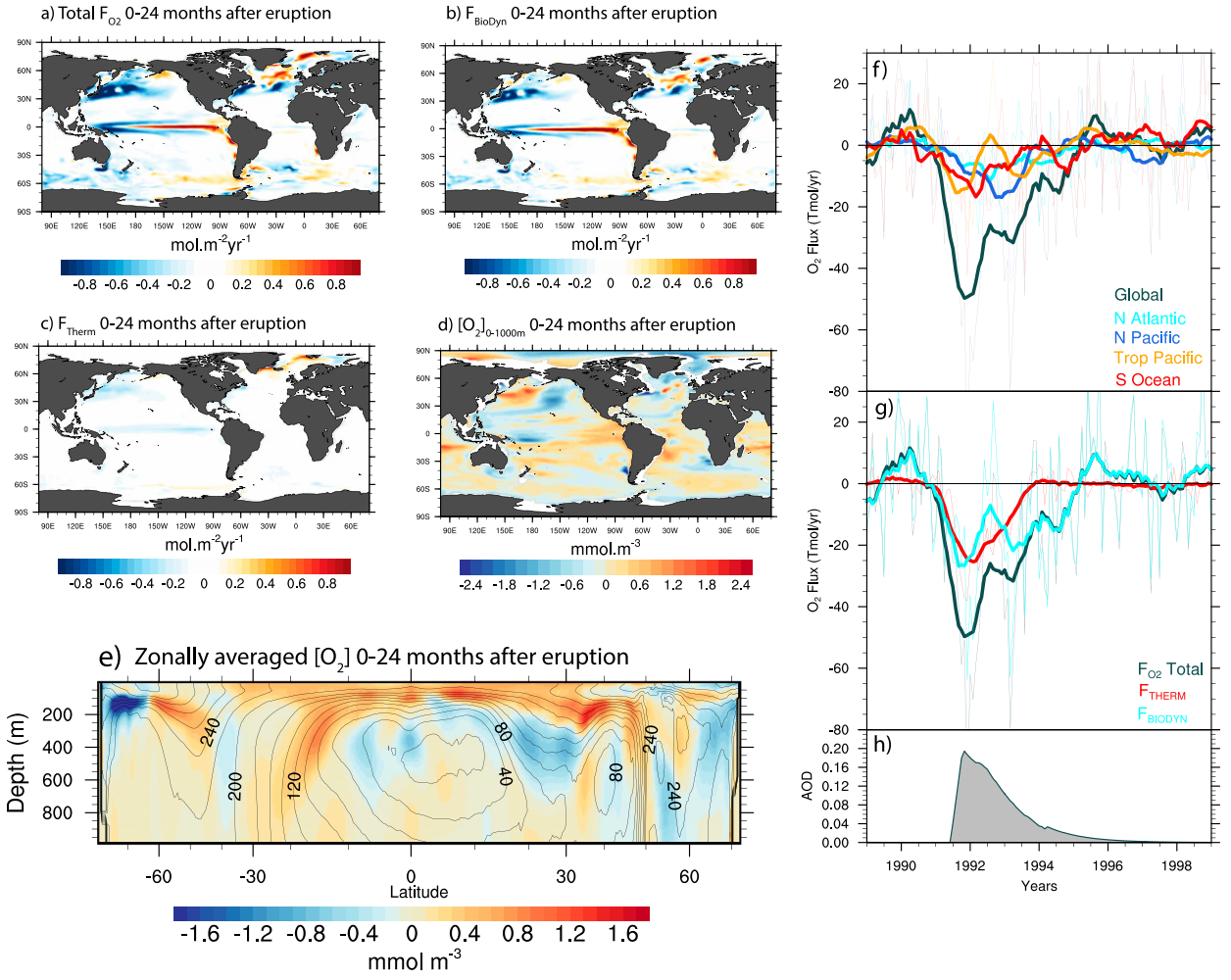

FIG. 10. CESM LE mean anomalies during 2 years following Pinatubo in (a) O_2 flux, decomposed by (b) biodynamical and (c) thermal contributions, (d) depth-averaged $[O_2]$ in the upper 0–1000-m ocean, and (e) zonally averaged $[O_2]$ change in the upper 1000 m (colors), with climatological $[O_2]$ in contours. (right) CESM LE mean global O_2 flux decomposition by (f) regional contributions and (g) process contributions. (h) Globally averaged 500-nm AOD. Spatial anomalies are calculated as annual mean anomalies during two years after eruption, with long-term linear trend removed. Thin lines indicate unfiltered series, while bold lines show 12-month running means. Positive flux denotes anomalous O_2 flux out of the ocean.

alkalinity (Alk), salinity (S), and freshwater fluxes (fw), following Takahashi et al. (1993) and Lovenduski et al. (2007), as

$$pCO_2' = \frac{\partial pCO_2}{\partial T}T' + \frac{\partial pCO_2}{\partial DIC}DIC' + \frac{\partial pCO_2}{\partial Alk}Alk' + \frac{\partial pCO_2}{\partial fw}fw' + \frac{\partial pCO_2}{\partial S}S', \quad (10)$$

where Alk and DIC are salinity-normalized to isolate the effects of freshwater on DIC and alkalinity.

Figures 11b and 11e show that DIC effects in the tropical Pacific dominate the simulated surface pCO_2 changes, in agreement with past studies of the carbon cycle response to El Niño (Feely et al. 2002; Long et al. 2013). This DIC influence is regionally counteracted by the alkalinity effects over the western Pacific and by weak warming effects along the equator, while pCO_2 changes due to freshwater fluxes and salinity effects are of minor importance. DIC effects, however, act in the opposite sense outside of the tropical Pacific, likely due to enhanced convection and upwelling at higher latitudes where they are largely canceled by strong cooling effects.

The El Niño–like response to Pinatubo explains most of the changes in the simulated global carbon uptake, as a deepened thermocline and reduced upwelling rates weaken DIC transport to the surface and suppress the outgassing of natural CO_2 in the tropical Pacific. The zonally averaged vertical DIC

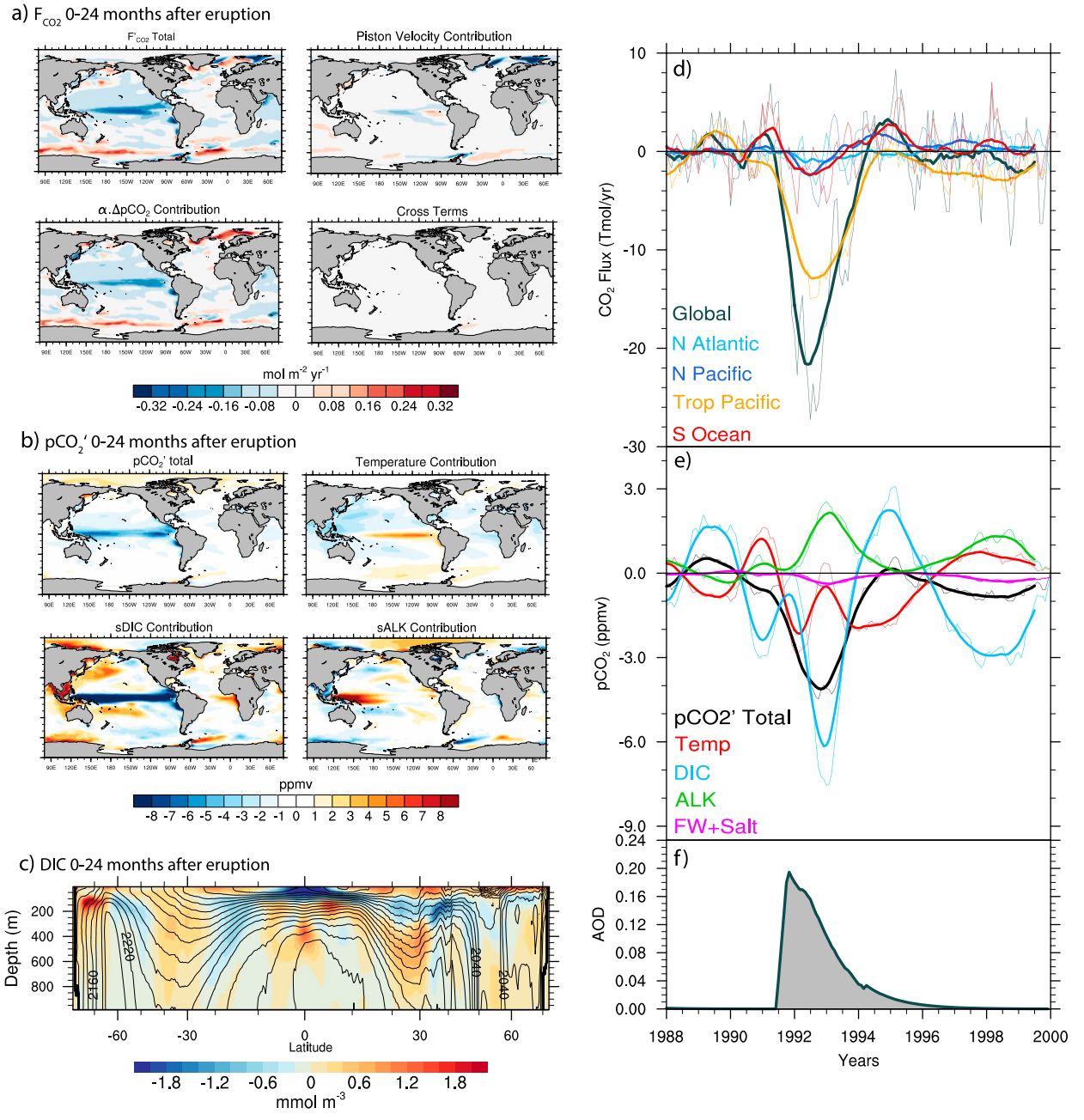

FIG. 11. CESM LE mean anomalies during 2 years following Pinatubo in (a) CO_2 flux decomposed by contributions from gas exchange piston velocity (PV′), $\Delta pCO_2'$, and cross terms, and (b) pCO_2 anomalies decomposed into thermal, DIC, and alkalinity contributions. (c) CESM LE mean anomalies in zonally averaged DIC with depth (color), averaged during the two years following eruption, with climatological DIC in contours. (d) Regional flux contributions, (e) process contributions to tropical Pacific pCO_2 anomalies including temperature, DIC, alkalinity, freshwater, and salinity effects, and (f) globally averaged 500-nm AOD. Spatial anomalies are calculated as annual mean anomalies during two years after eruption, with long-term linear trend removed. Thin lines indicate unfiltered series, while bold lines show 12-month running means. Positive flux denotes anomalous CO_2 flux out of the ocean.

anomalies shown in Fig. 11c reflect the effects of these dynamical processes and further indicate that positive anomalies in DIC occur primarily in the subtropical upper waters as anomalously undersaturated equatorial waters take up CO_2 and diverge poleward where cooling intensifies carbon uptake. Figure 11, thus, illustrates that volcanic eruptions lead to anomalous CO_2 uptake primarily through reduced tropical

Pacific outgassing of natural CO_2 via ENSO modulation of DIC transport to the surface.

6. Summary and discussion

In this study, we evaluate the physical and biogeochemical ocean response to tropical eruptions in the Large Ensemble suites of CESM and ESM2M. We find intense ocean cooling and O_2 and CO_2 uptake immediately follow eruptions in both models. These volcanic events act to significantly interrupt the advance of ocean warming, deoxygenation, and natural carbon loss in the ocean's interior, and drive pronounced interannual-to-decadal variability in ocean heat, O_2, and carbon fluxes and budgets. Distinct regional patterns emerge following tropical eruptions in both the CESM and ESM2M LE, with intensified convection and ventilation at higher latitudes and El Niño–like conditions in the tropical Pacific. This El Niño–like response 1) drives more ocean heat loss than is expected from the volcanic aerosols scattering effects alone, 2) dominates the global carbon uptake response through reducing natural tropical Pacific CO_2 outgassing, and 3) buffers the oceanic O_2 uptake at high latitudes through anomalous outgassing of O_2 along the equatorial Pacific, thus playing a major role in driving the physical and biogeochemical ocean response to tropical eruptions.

The tropical climate evolution following Pinatubo shown here may help reconcile the immediate cooling found in certain models (McGregor and Timmermann 2011) with the subsequent El Niño warming indicated by paleoproxies (Adams et al. 2003; Li et al. 2013). Initial cooling in the tropical Pacific, however, is short-lived and weak in the CESM LE whereas the El Niño warming is robust, similar to paleoproxy findings (Stevenson et al. 2017). This El Niño–like warming shown in CESM and ESM2M LE is in general agreement with recent findings by other models, including the Model for Interdisciplinary Research on Climate (MIROC; Ohba et al. 2013), Institut Pierre-Simon Laplace model (IPSL; Khodri et al. 2017), the ESM2M Climate Model, version 2.1 (CM2.1; Predybaylo et al. 2017), as well as the Last Millennium Ensemble (LME) experiment of CESM described in Stevenson et al. (2017). We note, however, that the peak El Niño warming occurs during boreal winter in CESM and ESM2M LE, consistent with a seasonally phased-locked response, rather than during boreal summer as found in other models (Khodri et al. 2017). We also note a relatively similar sensitivity of tropical Pacific climate response to ENSO phase during eruption year as found in previous studies (Ohba et al. 2013; Predybaylo et al. 2017; Khodri et al. 2017), with neutral and El Niño preconditioning promoting El Niño conditions a year following eruptions, whereas La Niña preconditioning is associated with a neutral (or an early termination of La Niña) response.

Whereas a coherent volcanic response of ENSO emerges across model-based and paleoproxy-based studies, proposed mechanisms remain at odds. Our results indicate that remote wind forcing from the western Pacific initiate surface equatorial warming in the eastern and central Pacific through downwelling equatorial Kelvin waves and the mean upwelling of warm subsurface anomalies (i.e., thermocline feedback). This initial surface warming is subsequently reinforced in the year following eruption through Bjerknes feedbacks as the zonal SST gradient is weakened, the easterlies relax, zonal advection is modified, and upwelling of cold thermocline waters is reduced, while other processes (e.g., meridional advection) play a minor role. This is in contrast to the dominance of the meridional advection feedback reported in the CESM LME (Stevenson et al. 2017) despite model similarity, signaling perhaps distinct processes for volcanic events of higher magnitudes or of different timing of eruption. Further work is needed to understand how processes governing the tropical Pacific climate response are influenced by the season and magnitude of eruption, as our study examines eruptions occurring during spring and summer (Table 1). We further note the dynamical mechanisms described in this study are largely similar to the MIROC results (Ohba et al. 2013) and IPSL results (Khodri et al. 2017), despite differences in models, magnitude of eruption, and methods for calculating anomalies.

We also stress that the remote wind forcing mechanism described in this study is distinct from the ocean dynamical thermostat, whereby upwelling of unperturbed waters buffers volcanic cooling and reduces the equatorial zonal SST gradient (Mann et al. 2005; Emile-Geay et al. 2008). In our study, significantly warmer waters, rather than ''pristine'' thermocline waters, are initially upwelled in the eastern and central equatorial Pacific promoting the initiation of El Niño through Bjerknes feedbacks. This subsurface warming is remotely forced by westerly wind anomalies over the western Pacific. Ohba et al. (2013) first reported the prevalence of these westerly wind anomalies following eruptions in MIROC, but proposed their role in ENSO through direct weakening of the Walker circulation. The subsurface temperature evolution shown in Fig. 8c suggests an oceanic link through the propagation of downwelling Kelvin waves that lead to the deepening of isotherms in the eastern and central equatorial Pacific, and the subsequent upwelling of warmer subsurface waters. This mechanism is in general agreement with the model findings of Khodri et al. (2017), who report similar westerly wind anomalies in

IPSL, but which they link to a weakening of the western African monsoon. We do not find major changes in atmospheric circulation over the African continent in either CESM or ESM2M (Fig. 8), suggesting instead a localized source for westerly wind anomalies potentially due to the advection of cold continental air from South Asia by the climatological winds to the Maritime Continent, and suppression of convection due to enhanced cooling over this region. The large and spatially complex anomalies found over the Indo-Pacific region in the year of eruption and the ocean–atmosphere and land–atmosphere interactions driving these westerly wind anomalies merit further investigation, ideally through a multimodel, regionally focused sensitivity study.

The CESM and ESM2M LE results also indicate a significant role for ocean dynamics in driving the biogeochemical response to tropical eruptions. This is especially evident in the anomalous CO_2 uptake following eruptions, which is driven here primarily by El Niño–induced deepening of the eastern and central equatorial Pacific thermocline and weakening of upwelling rates, rather than the temperature-dependent solubility effects as currently understood (Brovkin et al. 2010; Frölicher et al. 2011, 2013). The observed large anomalous CO_2 uptake after Pinatubo followed by a multiyear recovery in the observations-based flux estimate as well as in the hindcast and LE simulations of CESM (Fig. 5i) suggest that the Pinatubo perturbation of the oceanic carbon cycle may be a major driver of observed interannual to decadal variability in the global oceanic carbon sink. The simulated CO_2 flux response shown here, in turn, indicates a robust El Niño–like ocean response, even when the SST anomaly is ambiguous (i.e., Agung), providing similar insights gained from SSH anomalies that show El Niño–like patterns following eruptions in the absence of clear SST signals (Maher et al. 2015).

The volcanic impacts presented here have important implications for interpreting recently observed trends in the ocean. The strong volcanic modulation of oceanic O_2 in the northern subpolar and subtropical Pacific during the 1960s, 1980s, and 1990s, for instance, may have contributed to the well-observed bidecadal variability of $[O_2]$ in this region (Keeling et al. 2010). Similarly, the trend toward reduced carbon uptake during the recovery period (i.e., 1993–97) following Pinatubo found in both CESM and ESM2M LE (Fig. 5d) is in line with the weakening of the ocean carbon sink during the 1990s reported by recent synthesis of the SOCAT pCO_2 data (Landschützer et al. 2015) and in comparisons of WOCE-to-CLIVAR transects (Kouketsu et al. 2013) and WOCE-to-CLIVAR-to-GO-SHIP transects (Carter et al. 2017). In the context of the global decadal variability in air–sea CO_2 fluxes described by Landschützer et al. (2015), the signature of Pinatubo identified in ensemble-mean fluxes (Figs. 1d and 5d,i) needs to be taken into account as a forced component of observed decadal trends. In terms of process-attribution of this forced trend, the role of equatorial Pacific upwelling dynamics in modulating the CO_2 response indicates that an important component of the response is DIC-driven, in the framework of Feely et al. (2002), in addition to the expected SST-driven response over larger scales. We re-emphasize here the contrasting O_2 and CO_2 responses that originally drew our attention to the nonsolubility drivers of biogeochemical perturbations, underscoring the value of O_2 in guiding mechanistic insights into carbon cycle perturbations. In the case of CO_2, a more extensive and specific re-evaluation of a Pinatubo contribution to decadal variability in the equatorial Pacific (Takahashi et al. 2003; Feely et al. 2006; Landschützer et al. 2016) is left as a subject for future investigation.

Finally, enhanced ocean heat uptake is a leading explanation for the 2000–15 ''hiatus'' in global mean surface warming (Yan et al. 2016). While attention has been given primarily to anomalies in the 2000s decade, weaker ocean heat uptake in prior decades (1990s and 1980s) due to the integrated effects of the El Chichón and Pinatubo eruptions may also play a role in modulating decadal variability in the ocean heat content and surface trends. While evaluating the signature of volcanic events in interior ocean properties remain challenged by sparse sampling and large natural variability, the volcanic signals emerging in the CESM and ESM2M LE provide an important first step in identifying key patterns expected from volcanic forcing and relevant governing mechanisms. Finally, additional attribution studies following the LE framework, where volcanic perturbations are isolated from anthropogenic forcing are also clearly needed to identify the integrated effects of volcanic forcing on long-term trends in the ocean.

Acknowledgments. The authors are grateful for NSF and NCAR support. We would like to acknowledge high-performance computing support from Yellowstone (ark:/85065/d7wd3xhc) provided by NCAR's Computational and Information Systems Laboratory, sponsored by the National Science Foundation. This material is based on work supported by the National Science Foundation Graduate Research Fellowship under Grant DGE-1144086 for Y.A.E. The contribution of K.B.R. was supported by NASA Award NNX17AI75G and IBS-R028-D1. A.C.S. was supported for this research by a grant from NOAA Climate Variability and Prediction Program (NA14OAR4310276). The authors are grateful to Jeff Severinghaus, John Fasullo, and Sara Sanchez for valuable insights and discussions. The

Scripps O_2 program has been supported by a series of grants from the U.S. NSF and the NOAA, most recently Grants 1304270 and NA15OAR4320071. APO data are accessible on the Scripps Atmospheric Oxygen Research Program website at http://scrippso2.ucsd.edu/data. The SOCAT observations-based air–sea CO_2 flux estimates from the mixed layer scheme are archived in the MPI Jena website: https://www.bgc-jena.mpg.de/~christian.roedenbeck/. The CESM source code is freely available at http://www.cesm.ucar.edu. The model outputs described in this paper can be accessed at www.earthsystemgrid.org.

REFERENCES

Adams, J. B., M. E. Mann, and C. M. Ammann, 2003: Proxy evidence for an El Niño–like response to volcanic forcing. *Nature*, **426**, 274–278, https://doi.org/10.1038/nature02101.

Allan, R. P., C. Liu, N. G. Loeb, M. D. Palmer, M. Roberts, D. Smith, and P.-L. Vidale, 2014: Changes in global net radiative imbalance 1985–2012. *Geophys. Res. Lett.*, **41**, 5588–5597, https://doi.org/10.1002/2014GL060962.

Ammann, C. M., G. A. Meehl, W. M. Washington, and C. S. Zender, 2003: A monthly and latitudinally varying volcanic forcing dataset in simulations of 20th century climate. *Geophys. Res. Lett.*, **30**, 1657, https://doi.org/10.1029/2003GL016875.

Anderson, J. L., and Coauthors, 2004: The new GFDL global atmosphere and land model AM2–LM2: Evaluation with prescribed SST simulations. *J. Climate*, **17**, 4641–4673, https://doi.org/10.1175/JCLI-3223.1.

Balmaseda, M. A., K. E. Trenberth, and E. Källén, 2013: Distinctive climate signals in reanalysis of global ocean heat content. *Geophys. Res. Lett.*, **40**, 1754–1759, https://doi.org/10.1002/grl.50382.

Bopp, L., and Coauthors, 2013: Multiple stressors of ocean ecosystems in the 21st century: Projections with CMIP5 models. *Biogeosciences*, **10**, 6225–6245, https://doi.org/10.5194/bg-10-6225-2013.

Brovkin, V., S. J. Lorenz, J. Jungclaus, T. Raddatz, C. Timmreck, C. H. Reick, J. Segschneider, and K. Six, 2010: Sensitivity of a coupled climate–carbon cycle model to large volcanic eruptions during the last millennium. *Tellus*, **62B**, 674–681, https://doi.org/10.1111/j.1600-0889.2010.00471.x.

Carter, B., and Coauthors, 2017: Two decades of Pacific anthropogenic carbon storage and ocean acidification along Global Ocean Ship-Based Hydrographic Investigations Program sections p16 and p02. *Global Biogeochem. Cycles*, **31**, 306–327, https://doi.org/10.1002/2016GB005485.

Clement, A. C., R. Seager, M. A. Cane, and S. E. Zebiak, 1996: An ocean dynamical thermostat. *J. Climate*, **9**, 2190–2196, https://doi.org/10.1175/1520-0442(1996)009<2190:AODT>2.0.CO;2.

Danabasoglu, G., S. C. Bates, B. P. Briegleb, S. R. Jayne, M. Jochum, W. G. Large, S. Peacock, and S. G. Yeager, 2012: The CCSM4 ocean component. *J. Climate*, **25**, 1361–1389, https://doi.org/10.1175/JCLI-D-11-00091.1.

Delworth, T. L., V. Ramaswamy, and G. L. Stenchikov, 2005: The impact of aerosols on simulated ocean temperature and heat content in the 20th century. *Geophys. Res. Lett.*, **32**, L24709, https://doi.org/10.1029/2005GL024457.

Deser, C., A. Phillips, V. Bourdette, and H. Teng, 2012: Uncertainty in climate change projections: The role of internal variability. *Climate Dyn.*, **38**, 527–546, https://doi.org/10.1007/s00382-010-0977-x.

Ding, Y., J. A. Carton, G. A. Chepurin, G. Stenchikov, A. Robock, L. T. Sentman, and J. P. Krasting, 2014: Ocean response to volcanic eruptions in Coupled Model Intercomparison Project 5 simulations. *J. Geophys. Res. Oceans*, **119**, 5622–5637, https://doi.org/10.1002/2013JC009780.

Dunne, J. P., A. Gnanadesikan, J. L. Sarmiento, and R. D. Slater, 2010: Technical description of the prototype version (v0) of Tracers of Phytoplankton with Allometric Zooplankton (TOPAZ) ocean biogeochemical model as used in the Princeton IFMIP model. *Biogeosciences*, 7 (suppl.), 3595, https://www.biogeosciences.net/7/3593/2010/bg-7-3593-2010-supplement.pdf.

——, and Coauthors, 2012: GFDL's ESM2 global coupled climate–carbon Earth system models. Part I: Physical formulation and baseline simulation characteristics. *J. Climate*, **25**, 6646–6665, https://doi.org/10.1175/JCLI-D-11-00560.1.

——, and Coauthors, 2013: GFDL's ESM2 global coupled climate–carbon Earth system models. Part II: Carbon system formulation and baseline simulation characteristics. *J. Climate*, **26**, 2247–2267, https://doi.org/10.1175/JCLI-D-12-00150.1.

Dutton, E. G., and J. R. Christy, 1992: Solar radiative forcing at selected locations and evidence for global lower tropospheric cooling following the eruptions of El Chichón and Pinatubo. *Geophys. Res. Lett.*, **19**, 2313–2316, https://doi.org/10.1029/92GL02495.

Eddebbar, Y. A., M. C. Long, L. Resplandy, C. Rödenbeck, K. B. Rodgers, M. Manizza, and R. F. Keeling, 2017: Impacts of ENSO on air–sea oxygen exchange: Observations and mechanisms. *Global Biogeochem. Cycles*, **31**, 901–921, https://doi.org/10.1002/2017GB005630.

Emile-Geay, J., R. Seager, M. A. Cane, E. R. Cook, and G. H. Haug, 2008: Volcanoes and ENSO over the past millennium. *J. Climate*, **21**, 3134–3148, https://doi.org/10.1175/2007JCLI1884.1.

Feely, R. A., and Coauthors, 2002: Seasonal and interannual variability of CO_2 in the equatorial Pacific. *Deep-Sea Res. II*, **49**, 2443–2469, https://doi.org/10.1016/S0967-0645(02)00044-9.

——, T. Takahashi, R. Wanninkhof, M. McPhaden, C. Cosca, S. Sutherland, and M.-E. Carr, 2006: Decadal variability of the air–sea CO_2 fluxes in the equatorial Pacific Ocean. *J. Geophys. Res.*, **111**, C08S90, https://doi.org/10.1029/2005JC003129.

Frölicher, T. L., F. Joos, G.-K. Plattner, M. Steinacher, and S. C. Doney, 2009: Natural variability and anthropogenic trends in oceanic oxygen in a coupled carbon cycle–climate model ensemble. *Global Biogeochemical Cycles*, **23**, GB1003, https://doi.org/10.1029/2008GB003316.

——, ——, and C. C. Raible, 2011: Sensitivity of atmospheric CO_2 and climate to explosive volcanic eruptions. *Biogeosciences*, **8**, 2317–2339, https://doi.org/10.5194/bg-8-2317-2011.

——, ——, ——, and J. L. Sarmiento, 2013: Atmospheric CO_2 response to volcanic eruptions: The role of ENSO, season, and variability. *Global Biogeochem. Cycles*, **27**, 239–251, https://doi.org/10.1002/gbc.20028.

Gao, C., A. Robock, and C. Ammann, 2008: Volcanic forcing of climate over the past 1500 years: An improved ice core-based index for climate models. *J. Geophys. Res.*, **113**, D23111, https://doi.org/10.1029/2008JD010239.

Gill, A., 1980: Some simple solutions for heat-induced tropical circulation. *Quart. J. Roy. Meteor. Soc.*, **106**, 447–462, https://doi.org/10.1002/qj.49710644905.

Gleckler, P. J., K. M. AchutaRao, J. M. Gregory, B. D. Santer, K. E. Taylor, and T. M. L. Wigley, 2006: Krakatoa lives: The effect of volcanic eruptions on ocean heat content and thermal expansion. *Geophys. Res. Lett.*, **33**, L17702, https://doi.org/10.1029/2006GL026771.

Griffies, S. M., M. Schmidt, and M. Herzfeld, 2009: Elements of MOM4p1. GFDL Ocean Group Tech. Rep. 6, 444 pp.

Huang, B., Y. Xue, D. Zhang, A. Kumar, and M. J. McPhaden, 2010: The NCEP GODAS ocean analysis of the tropical Pacific mixed layer heat budget on seasonal to interannual time scales. *J. Climate*, **23**, 4901–4925, https://doi.org/10.1175/2010JCLI3373.1.

Hunke, E., W. Lipscomb, A. Turner, N. Jeffery, and S. Elliott, 2008: CICE: The Los Alamos Sea Ice Model, documentation and software, version 4.0. Los Alamos National Laboratory Tech. Rep. LA-CC-06-012, 76 pp.

Hurrell, J. W., and Coauthors, 2013: The Community Earth System Model: A framework for collaborative research. *Bull. Amer. Meteor. Soc.*, **94**, 1339–1360, https://doi.org/10.1175/BAMS-D-12-00121.1.

Ito, T., S. Minobe, M. C. Long, and C. Deutsch, 2017: Upper ocean O_2 trends: 1958–2015. *Geophys. Res. Lett.*, **44**, 4214–4223, https://doi.org/10.1002/2017GL073613.

Kay, J. E., and Coauthors, 2015: The Community Earth System Model (CESM) Large Ensemble Project: A community resource for studying climate change in the presence of internal climate variability. *Bull. Amer. Meteor. Soc.*, **96**, 1333–1349, https://doi.org/10.1175/BAMS-D-13-00255.1.

Keeling, R. F., and A. Manning, 2014: Studies of recent changes in atmospheric O_2 content. *Treatise on Geochemistry*, Vol. 5, Elsevier, 385–404.

——, R. P. Najjar, M. L. Bender, and P. P. Tans, 1993: What atmospheric oxygen measurements can tell us about the global carbon cycle. *Global Biogeochem. Cycles*, **7**, 37–67, https://doi.org/10.1029/92GB02733.

——, A. Körtzinger, and N. Gruber, 2010: Ocean deoxygenation in a warming world. *Annu. Rev. Mar. Sci.*, **2**, 199–229, https://doi.org/10.1146/annurev.marine.010908.163855.

Khodri, M., and Coauthors, 2017: Tropical explosive volcanic eruptions can trigger El Niño by cooling tropical Africa. *Nat. Commun.*, **8**, 778, https://doi.org/10.1038/s41467-017-00755-6.

Kouketsu, S., A. Murata, and T. Doi, 2013: Decadal changes in dissolved inorganic carbon in the Pacific Ocean. *Global Biogeochem. Cycles*, **27**, 65–76, https://doi.org/10.1029/2012GB004413.

Lamb, H., 1983: Update of the chronology of assessments of the volcanic dust veil index. *Climate Monitor,* **12** (3), 79–90.

Landschützer, P., and Coauthors, 2015: The reinvigoration of the Southern Ocean carbon sink. *Science*, **349**, 1221–1224, https://doi.org/10.1126/science.aab2620.

——, N. Gruber, and D. C. Bakker, 2016: Decadal variations and trends of the global ocean carbon sink. *Global Biogeochem. Cycles*, **30**, 1396–1417, https://doi.org/10.1002/2015GB005359.

Lehner, F., A. P. Schurer, G. C. Hegerl, C. Deser, and T. L. Frölicher, 2016: The importance of ENSO phase during volcanic eruptions for detection and attribution. *Geophys. Res. Lett.*, **43**, 2851–2858, https://doi.org/10.1002/2016GL067935.

Li, J., and Coauthors, 2013: El Niño modulations over the past seven centuries. *Nat. Climate Change*, **3**, 822–826, https://doi.org/10.1038/nclimate1936.

Liu, C., and Coauthors, 2015: Combining satellite observations and reanalysis energy transports to estimate global net surface energy fluxes 1985–2012. *J. Geophys. Res.*, **120**, 9374–9389, https://doi.org/10.1002/2015JD023264.

Liu, F., J. Li, B. Wang, J. Liu, T. Li, G. Huang, and Z. Wang, 2018: Divergent El Niño responses to volcanic eruptions at different latitudes over the past millennium. *Climate Dyn.*, **50**, 3799–3812, https://doi.org/10.1007/s00382-017-3846-z.

Long, M. C., K. Lindsay, S. Peacock, J. K. Moore, and S. C. Doney, 2013: Twentieth-century oceanic carbon uptake and storage in CESM1 (BGC). *J. Climate*, **26**, 6775–6800, https://doi.org/10.1175/JCLI-D-12-00184.1.

——, C. A. Deutsch, and T. Ito, 2016: Finding forced trends in oceanic oxygen. *Global Biogeochem. Cycles*, **30**, 381–397, https://doi.org/10.1002/2015GB005310.

Lovenduski, N. S., N. Gruber, S. C. Doney, and I. D. Lima, 2007: Enhanced CO_2 outgassing in the Southern Ocean from a positive phase of the southern annular mode. *Global Biogeochem. Cycles*, **21**, GB2026, https://doi.org/10.1029/2006GB002900.

Maher, N., S. McGregor, M. H. England, and A. Sen Gupta, 2015: Effects of volcanism on tropical variability. *Geophys. Res. Lett.*, **42**, 6024–6033, https://doi.org/10.1002/2015GL064751.

Mann, M. E., M. A. Cane, S. E. Zebiak, and A. Clement, 2005: Volcanic and solar forcing of the tropical Pacific over the past 1000 years. *J. Climate*, **18**, 447–456, https://doi.org/10.1175/JCLI-3276.1.

McGregor, S., and A. Timmermann, 2011: The effect of explosive tropical volcanism on ENSO. *J. Climate*, **24**, 2178–2191, https://doi.org/10.1175/2010JCLI3990.1.

McKinley, G. A., D. J. Pilcher, A. R. Fay, K. Lindsay, M. C. Long, and N. Lovenduski, 2016: Timescales for detection of trends in the ocean carbon sink. *Nature*, **530**, 469–472, https://doi.org/10.1038/nature16958.

Moore, J. K., K. Lindsay, S. C. Doney, M. C. Long, and K. Misumi, 2013: Marine ecosystem dynamics and biogeochemical cycling in the Community Earth System Model [CESM1 (BGC)]: Comparison of the 1990s with the 2090s under the RCP4.5 and RCP8.5 scenarios. *J. Climate*, **26**, 9291–9312, https://doi.org/10.1175/JCLI-D-12-00566.1.

Ohba, M., H. Shiogama, T. Yokohata, and M. Watanabe, 2013: Impact of strong tropical volcanic eruptions on ENSO simulated in a coupled GCM. *J. Climate*, **26**, 5169–5182, https://doi.org/10.1175/JCLI-D-12-00471.1.

Pausata, F. S., C. Karamperidou, R. Caballero, and D. S. Battisti, 2016: ENSO response to high-latitude volcanic eruptions in the Northern Hemisphere: The role of the initial conditions. *Geophys. Res. Lett.*, **43**, 8694–8702, https://doi.org/10.1002/2016GL069575.

Pollack, J. B., O. B. Toon, C. Sagan, A. Summers, B. Baldwin, and W. Van Camp, 1976: Volcanic explosions and climatic change: A theoretical assessment. *J. Geophys. Res.*, **81**, 1071–1083, https://doi.org/10.1029/JC081i006p01071.

Predybaylo, E., G. L. Stenchikov, A. T. Wittenberg, and F. Zeng, 2017: Impacts of a Pinatubo-size volcanic eruption on ENSO. *J. Geophys. Res.*, **122**, 925–947, https://doi.org/10.1002/2016JD025796.

Rampino, M. R., and S. Self, 1982: Historic eruptions of Tambora (1815), Krakatau (1883), and Agung (1963), their stratospheric aerosols, and climatic impact. *Quat. Res.*, **18**, 127–143, https://doi.org/10.1016/0033-5894(82)90065-5.

Rayner, N., D. E. Parker, E. Horton, C. Folland, L. Alexander, D. Rowell, E. Kent, and A. Kaplan, 2003: Global analyses of sea surface temperature, sea ice, and night marine air temperature since the late nineteenth century. *J. Geophys. Res.*, **108**, 4407, https://doi.org/10.1029/2002JD002670.

Reynolds, R. W., N. A. Rayner, T. M. Smith, D. C. Stokes, and W. Wang, 2002: An improved in situ and satellite SST analysis

for climate. *J. Climate*, **15**, 1609–1625, https://doi.org/10.1175/1520-0442(2002)015<1609:AIISAS>2.0.CO;2.

Robock, A., 2000: Volcanic eruptions and climate. *Rev. Geophys.*, **38**, 191–219, https://doi.org/10.1029/1998RG000054.

——, and M. P. Free, 1996: The volcanic record in ice cores for the past 2000 years. *Climatic Variations and Forcing Mechanisms of the Last 2000 Years,* P. D. Jones, R. S. Bradley, and J. Jouzel, Eds., Springer, 533–546.

Rödenbeck, C., and Coauthors, 2014: Interannual sea–air CO_2 flux variability from an observation-driven ocean mixed-layer scheme. *Biogeosciences*, **11**, 4599–4613, https://doi.org/10.5194/bgd-11-3167-2014.

Rodgers, K., J. Lin, and T. Frölicher, 2015: Emergence of multiple ocean ecosystem drivers in a large ensemble suite with an Earth system model. *Biogeosciences*, **12**, 3301–3320, https://doi.org/10.5194/bg-12-3301-2015.

Santer, B. D., and Coauthors, 2014: Volcanic contribution to decadal changes in tropospheric temperature. *Nat. Geosci.*, **7**, 185–189, https://doi.org/10.1038/ngeo2098.

Sarmiento, J., 1993: Atmospheric CO_2 stalled. *Nature*, **365**, 697–698, https://doi.org/10.1038/365697a0.

Sato, M., J. E. Hansen, M. P. McCormick, and J. B. Pollack, 1993: Stratospheric aerosol optical depths, 1850–1990. *J. Geophys. Res.*, **98**, 22 987–22 994, https://doi.org/10.1029/93JD02553.

Schmidtko, S., L. Stramma, and M. Visbeck, 2017: Decline in global oceanic oxygen content during the past five decades. *Nature*, **542**, 335–339, https://doi.org/10.1038/nature21399.

Schneider, D. P., C. M. Ammann, B. L. Otto-Bliesner, and D. S. Kaufman, 2009: Climate response to large, high-latitude and low-latitude volcanic eruptions in the Community Climate System Model. *J. Geophys. Res.*, **114**, D15101, https://doi.org/10.1029/2008JD011222.

Segschneider, J., and Coauthors, 2013: Impact of an extremely large magnitude volcanic eruption on the global climate and carbon cycle estimated from ensemble Earth system model simulations. *Biogeosciences*, **10**, 669–687, https://doi.org/10.5194/bg-10-669-2013.

Severinghaus, J. P., 1995: Studies of the terrestrial O_2 and carbon cycles in sand dune gases and in biosphere 2. Ph.D. thesis, Columbia University, 148 pp., https://doi.org/10.2172/477735.

Simkin, T., and L. Siebert, 1994: *Volcanoes of the World.* Geoscience Press, 349 pp.

Slawinska, J., and A. Robock, 2018: Impact of volcanic eruptions on decadal to centennial fluctuations of Arctic sea ice extent during the last millennium and on initiation of the Little Ice Age. *J. Climate*, **31**, 2145–2167, https://doi.org/10.1175/JCLI-D-16-0498.1.

Stenchikov, G. L., I. Kirchner, A. Robock, H.-F. Graf, J. C. Antuña, R. G. Grainger, A. Lambert, and L. Thomason, 1998: Radiative forcing from the 1991 Mount Pinatubo volcanic eruption. *J. Geophys. Res.*, **103**, 13 837–13 857, https://doi.org/10.1029/98JD00693.

——, K. Hamilton, R. J. Stouffer, A. Robock, V. Ramaswamy, B. Santer, and H.-F. Graf, 2006: Arctic oscillation response to volcanic eruptions in the IPCC AR4 climate models. *J. Geophys. Res.*, **111**, D07107, https://doi.org/10.1029/2005JD006286.

Stenchikov, G., T. L. Delworth, V. Ramaswamy, R. J. Stouffer, A. Wittenberg, and F. Zeng, 2009: Volcanic signals in oceans. *J. Geophys. Res.*, **114**, D16104, https://doi.org/10.1029/2008JD011673.

Stephens, B. B., R. F. Keeling, M. Heimann, K. D. Six, R. Murnane, and K. Caldeira, 1998: Testing global ocean carbon cycle models using measurements of atmospheric O_2 and CO_2 concentration. *Global Biogeochem. Cycles*, **12**, 213–230, https://doi.org/10.1029/97GB03500.

Stevenson, S., J. T. Fasullo, B. L. Otto-Bliesner, R. A. Tomas, and C. Gao, 2017: Role of eruption season in reconciling model and proxy responses to tropical volcanism. *Proc. Natl. Acad. Sci. USA*, **114**, 1822–1826, https://doi.org/10.1073/pnas.1612505114.

Takahashi, T., J. Olafsson, J. G. Goddard, D. W. Chipman, and S. Sutherland, 1993: Seasonal variation of CO_2 and nutrients in the high-latitude surface oceans: A comparative study. *Global Biogeochem. Cycles*, **7**, 843–878, https://doi.org/10.1029/93GB02263.

——, S. C. Sutherland, R. A. Feely, and C. E. Cosca, 2003: Decadal variation of the surface water pCO_2 in the western and central equatorial Pacific. *Science*, **302**, 852–856, https://doi.org/10.1126/science.1088570.

Trenberth, K. E., 1997: The definition of El Niño. *Bull. Amer. Meteor. Soc.*, **78**, 2771–2778, https://doi.org/10.1175/1520-0477(1997)078<2771:TDOENO>2.0.CO;2.

Wanninkhof, R., 1992: Relationship between wind speed and gas exchange over the ocean. *J. Geophys. Res.*, **97**, 7373–7382, https://doi.org/10.1029/92JC00188.

Xie, S.-P., C. Deser, G. A. Vecchi, J. Ma, H. Teng, and A. T. Wittenberg, 2010: Global warming pattern formation: Sea surface temperature and rainfall. *J. Climate*, **23**, 966–986, https://doi.org/10.1175/2009JCLI3329.1.

Yan, X.-H., T. Boyer, K. Trenberth, T. R. Karl, S.-P. Xie, V. Nieves, K.-K. Tung, and D. Roemmich, 2016: The global warming hiatus: Slowdown or redistribution? *Earth's Future*, **4**, 472–482, https://doi.org/10.1002/2016EF000417.

Zanchettin, D., C. Timmreck, H.-F. Graf, A. Rubino, S. Lorenz, K. Lohmann, K. Krüger, and J. Jungclaus, 2012: Bi-decadal variability excited in the coupled ocean–atmosphere system by strong tropical volcanic eruptions. *Climate Dyn.*, **39**, 419–444, https://doi.org/10.1007/s00382-011-1167-1.